19.6. Electron cryomicroscopy

BY T. S. BAKER AND R. HENDERSON

19.6.1. Abbreviations used

0D	Zero-dimensional (single particles)
1D	One-dimensional (helical)
2D	Two-dimensional
3D	Three-dimensional
EM	Electron microscope/microscopy
Cryo EM	Electron cryomicroscopy
FEG	Field-emission gun
CTF	Contrast-transfer function
CCD	Charge-coupled device (slow-scan TV detector)

19.6.2. The role of electron microscopy in macromolecular structure determination

Diffraction and imaging techniques are one manifestation of the use of scattering of beams or wavefronts by objects to analyse the structure of that object (Fig. 19.6.2.1). Such methods can be used in general for the examination of structures of any size, ranging from elementary subnuclear particles all the way up to the structure of the earth's core. For macromolecular structure determination, there are two main differences between the use of electrons and X-rays to probe structure. The most important is that the scattering cross section is about 10^5 times greater for electrons than it is for X-rays, so significant scattering using electrons is obtained for crystals or other specimens that are 1 to 10 nm thick, whereas scattering or absorption of a similar fraction of an illuminating X-ray beam requires crystals that are 100 to 500 μm thick. The second main difference is that electrons are much more easily focused than X-rays since they are charged particles that can be deflected by electric or magnetic fields. As a result, electron lenses are much superior to X-ray lenses and can be used to produce a magnified image of an object as easily as a diffraction pattern. This then allows the electron microscope to be switched back and forth instantly between imaging and diffraction modes so that the image of a single molecule at any magnification can be obtained as conveniently as the electron diffraction pattern of a thin crystal. By contrast, X-ray microscopy has been much less valuable than X-ray diffraction, but may be useful for imaging at the cellular level.

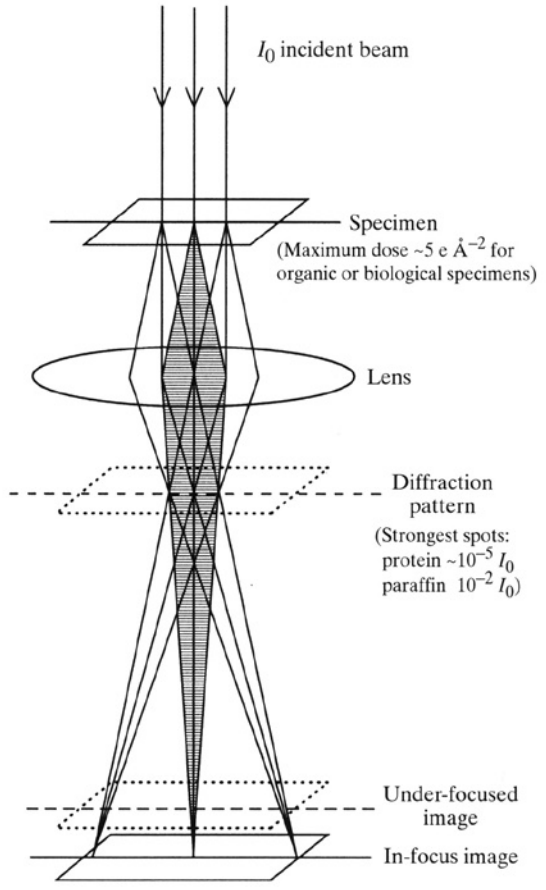

Fig. 19.6.2.1. Schematic diagram showing the principle of image formation and diffraction in the transmission electron microscope. The incident beam, I_0, illuminates the specimen. Scattered and unscattered electrons are collected by the objective lens and focused back to form first an electron-diffraction pattern and then an image. For a 2D or 3D crystal, the electron-diffraction pattern would show a lattice of spots, each of whose intensity is a small fraction of that of the incident beam. In practice, an in-focus image has virtually no contrast, so images are recorded with the objective lens slightly defocused to take advantage of the out-of-focus phase-contrast mechanism.

In the early years of electron microscopy of macromolecules, electron micrographs of molecules embedded in a thin film of heavy-atom stains (Brenner & Horne, 1959; Huxley & Zubay, 1960) were used to produce pictures which were interpreted directly. Beginning with the work of Klug (Klug & Berger, 1964), a more rigorous approach to image analysis led first to the interpretation of the two-dimensional (2D) images as the projected density summed along the direction of view and then to the ability to reconstruct the three-dimensional (3D) object from which the images arose (DeRosier & Klug, 1968; Hoppe *et al.*, 1968), with subsequent more sophisticated treatment of image contrast transfer (Erickson & Klug, 1971).

Later, macromolecules were examined by electron diffraction and imaging without the use of heavy-atom stains by embedding the specimens in either a thin film of glucose (Unwin & Henderson, 1975) or in a thin film of rapidly (Dubochet, Lepault *et al.*, 1982; Dubochet *et al.*, 1988) or slowly (Taylor & Glaeser, 1974) frozen water, which required the specimen to be cooled while it was examined in the electron microscope. This use of unstained specimens thus led to the structure determination of the molecules themselves, rather than the structure of a 'negative stain' excluding volume, and has created the burgeoning field of 3D electron microscopy of macromolecules. Many of the image-analysis techniques now used for studying unstained specimens originated from those used in the analysis of negatively stained samples.

At this point in year 2000, hundreds of medium-resolution structures of macromolecular assemblies (*e.g.* ribosomes), spherical and helical viruses, and larger protein molecules have been determined by electron cryomicroscopy in ice. Three atomic resolution structures have been obtained by electron cryomicroscopy of thin 2D crystals embedded in glucose, trehalose or tannic acid (Henderson *et al.*, 1990; Kühlbrandt *et al.*, 1994; Nogales *et al.*, 1998), where specimen cooling reduced the effect of radiation damage. The medium-resolution density distributions can often be interpreted in terms of the chemistry of the structure if a high-resolution model of one or more of the component pieces has already been obtained by X-ray, electron microscopy, or NMR methods. As a result, electron microscopy is being transformed from a niche methodology into a powerful technique for which, in some cases, no alternative approach is possible. This article outlines the key aspects of electron cryomicroscopy (cryo EM) and 3D image reconstruction. Further information can be obtained from several reviews (*e.g.* Amos *et al.*, 1982; Glaeser, 1985; Chiu, 1986;

Dubochet *et al.*, 1988; Stewart, 1990; Koster *et al.*, 1997; Walz & Grigorieff, 1998; Baker *et al.*, 1999; Yeager *et al.*, 1999) and a book (Frank, 1996). Recommended textbooks that describe general aspects of electron microscopy are those by Cowley (1975), Spence (1988) and Reimer (1989).

19.6.3. Electron scattering and radiation damage

A schematic overview of scattering and imaging in the electron microscope is depicted in Fig. 19.6.2.1. For biological electron microscopy and diffraction, the incident beam is normally parallel and monochromatic. The incident electron beam then passes through the specimen and individual electrons are either unscattered or scattered by the atoms of the specimen. This scattering occurs either elastically, with no loss of energy and therefore no energy deposition in the specimen, or inelastically, with consequent energy loss by the scattered electron and accompanying energy deposition in the specimen, resulting in radiation damage. The electrons emerging from the specimen are then collected by the imaging optics, shown here for simplicity as a single lens, but in practice consisting of a complex system of five or six lenses with intermediate images being produced at successively higher magnification at different positions down the column. Finally, in the viewing area, either the electron-diffraction pattern or the image can be seen directly by eye on the phosphor screen, or detected by a TV or CCD camera, or recorded on photographic film or an image plate.

19.6.3.1. *Elastic and inelastic scattering*

The coherent, elastically scattered electrons contain all the high-resolution information describing the structure of the specimen. The amplitudes and phases of the scattered electron beams are directly related to the amplitudes and phases of the Fourier components of the atomic distribution in the specimen. When the scattered beams are recombined with the unscattered beam in the image, they create an interference pattern (the image) which, for thin specimens, is related approximately linearly to the density variations in the specimen. The information about the structure of the specimen can then be retrieved by digitization and computer-based image processing, as described below (Sections 19.6.4.5 and 19.6.4.6). The elastic scattering cross sections for electrons are not as simply related to the atomic composition as happens with X-rays. With X-ray diffraction, the scattering factors are simply proportional to the number of electrons in each atom, normally equal to the atomic number. Since elastically scattered electrons are in effect diffracted by the electrical potential inside atoms, the scattering factor for electrons depends not only on the nuclear charge but also on the size of the surrounding electron cloud which screens the nuclear charge. As a result, electron scattering factors in the resolution range of interest in macromolecular structure determination (up to $\frac{1}{3}$ Å^{-1}) are very sensitive to the effective radius of the outer valency electrons and therefore depend sensitively on the chemistry of bonding. Although this is a fascinating field in itself with interesting work already carried out by the gas-phase electron-diffraction community (*e.g.* Hargittai & Hargittai, 1988), it is still an area where much work remains to be done. At present, it is probably adequate to think of the density obtained in macromolecular structure analysis by electron microscopy as roughly equivalent to the electron density obtained by X-ray diffraction but with the contribution from hydrogen atoms being somewhat greater relative to carbon, nitrogen and oxygen.

Those electrons which are inelastically scattered lose energy to the specimen by a number of mechanisms. The energy-loss spectrum for a typical biological specimen is dominated by the large cross section for plasmon scattering in the energy range 20–30 eV with a continuum in the distribution which decreases up to higher energies. At discrete high energies, specific inner electrons in the *K* shell of carbon, nitrogen or oxygen can be ejected with corresponding peaks in the energy-loss spectrum appearing at 200–400 eV. Any of these inelastic interactions produces an uncertainty in the position of the scattered electron (by Heisenberg's uncertainty principle) and as a result, the resolution of any information present in the energy-loss electron signal extends only to low resolutions of around 15 Å (Isaacson *et al.*, 1974). Consequently, the inelastically scattered electrons are generally considered to contribute little except noise to the images.

19.6.3.2. *Radiation damage*

The most important consequence of inelastic scattering is the deposition of energy into the specimen. This is initially transferred to secondary electrons which have an average energy (20 eV) that is five or ten times greater than the valency bond energies. These secondary electrons interact with other components of the specimen and produce numerous reactive chemical species, including free radicals. In ice-embedded samples, these would be predominantly highly reactive hydroxyl free radicals that arise from the frozen water molecules. In turn, these react with the embedded macromolecules and create a great variety of radiation products such as modified side chains, cleaved polypeptide backbones and a host of molecular fragments. From radiation-chemistry studies, it is known that thiol or disulfide groups react more quickly than aliphatic groups and that aromatic groups, including nucleic acid bases, are the most resistant. Nevertheless, the end effect of the inelastic scattering is the degradation of the specimen to produce a cascade of heterogeneous products, some of which resemble the starting structure more closely than others. Some of the secondary electrons also escape from the surface of the specimen, causing it to charge up during the exposure. As a rough rule, for 100 kV electrons the dose that can be used to produce an image in which the starting structure at high resolution is still recognizable is about 1 e Å^{-2} for organic or biological materials at room temperature, 5 e Å^{-2} for a specimen near liquid-nitrogen temperature (−170 °C) and 10 e Å^{-2} for a specimen near liquid-helium temperature (4–8 K). However, individual experimenters will often exceed these doses if they wish to enhance the low-resolution information in the images, which is less sensitive to radiation damage. The effects of radiation damage due to electron irradiation are essentially identical to those from X-ray or neutron irradiation for biological macromolecules except for the amount of energy deposition per useful coherent elastically scattered event (Henderson, 1995). For electrons scattered by biological structures at all electron energies of interest, the number of inelastic events exceeds the number of elastic events by a factor of three to four, so that 60 to 80 eV of energy is deposited for each elastically scattered electron. This limits the amount of information in an image of a single biological macromolecule. Consequently, the 3D atomic structure cannot be determined from a single molecule but requires the averaging of the information from at least 10000 molecules in theory, and even more in practice (Henderson, 1995). Crystals used for X-ray or neutron diffraction contain many orders of magnitude more molecules.

It is possible to collect both the elastically and the inelastically scattered electrons simultaneously with an energy analyser and, if a fine electron beam is scanned over the specimen, then a scanning transmission electron micrograph displaying different properties of the specimen can be obtained. Alternatively, conventional transmission electron microscopes to which an energy filter has been added can be used to select out a certain energy band of the electrons from the image. Both these types of microscope can contribute in other ways to the knowledge of structure, but in this article, we concentrate on high-voltage phase-contrast electron microscopy

of unstained macromolecules most often embedded in ice, because this is the method of widest impact and whose results encompass all resolutions both complementary to and competitive with those from X-ray diffraction.

19.6.3.3. *Required properties of the illuminating electron beam*

The important properties of the image in terms of defocus, astigmatism and the presence and effect of amplitude or phase contrast are discussed below (Sections 19.6.4.4 and 19.6.4.6). The best-quality incident electron beam is produced by a field emission gun (FEG). This is because the electrons from a FEG are emitted from a very small volume at the tip, which is the apparent source size. Once these electrons have been collected by the condenser lens and used to produce the illuminating beam, that beam of electrons is then very parallel (divergence of $\sim 10^{-2}$ mrad) and therefore spatially coherent. Similarly, because the emitting tip of a FEG is not heated as much as a conventional thermionic tungsten source, the thermal energy spread of the electrons is relatively small (0.5 to 1.0 eV) and, as a result, the illuminating beam is monochromatic and therefore temporally coherent. Electron beams can also be produced by a normal heated tungsten source, which gives a less parallel beam with a larger energy spread, but is nevertheless adequate for electron cryomicroscopy if the highest resolution images are not required.

19.6.4. Three-dimensional electron cryomicroscopy of macromolecules

The determination of 3D structure by cryo EM methods follows a common scheme for all macromolecules (Fig. 19.6.4.1). A more detailed discussion of the individual steps as applied to different classes of macromolecules appears in subsequent sections. Briefly, each specimen must be prepared in a relatively homogeneous aqueous form (1D or 2D crystals or a suspension of single particles in a limited number of states) at relatively high concentration, rapidly frozen (vitrified) as a thin film, transferred into the electron microscope and photographed by means of low-dose selection and focusing procedures. The resulting images, if recorded on film, must then be digitized. Digitized images are then processed using a series of computer programs that allow different views of the specimen to be combined into a 3D reconstruction that can be interpreted in terms of other available structural, biochemical and molecular data.

19.6.4.1. *Overview of conceptual steps*

Radiation damage by the illuminating electron beam generally allows only one good picture (micrograph) to be obtained from each molecule or macromolecular assembly. In this micrograph, the signal-to-noise ratio of the 2D projection image is normally too small to determine the projected structure accurately. This implies firstly that it is necessary to average many images of different molecules taken from essentially the same viewpoint to increase the signal-to-noise ratio, and secondly that many of these averaged projections, taken from different directions, must be combined to build up the information necessary to determine the 3D structure of the molecule. Thus, the two key concepts are: (1) averaging to a greater or lesser extent depending on resolution, particle size and symmetry to increase the signal-to-noise ratio; and (2) the combination of different projections to build a 3D map of the structure.

In addition, there are various technical corrections that must be made to the image data to allow an unbiased model of the structure to be obtained. These include correction for the phase contrast-transfer function (CTF – see Fig. 19.6.4.4 in Section 19.6.4.4 for a description of the CTF and Section 19.6.4.6 for its correction) and for the effects of beam tilt. For crystals, it is also possible to combine electron-diffraction amplitudes with image phases to produce a more accurate structure (Unwin & Henderson, 1975), and in general to correct for loss of high-resolution contrast for any reason by 'sharpening' the data by application of a negative temperature factor (Havelka *et al.*, 1995).

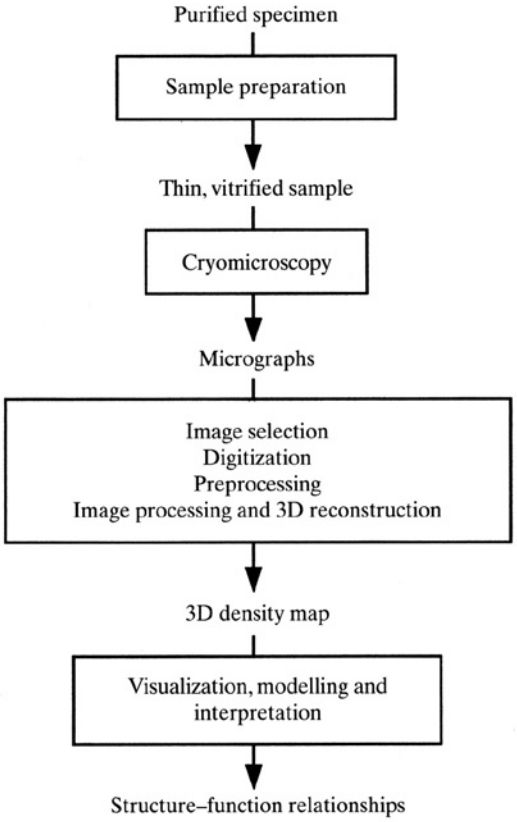

Fig. 19.6.4.1. Flow diagram showing all the procedures involved in electron cryomicroscopy from sample preparation to map interpretation. Each of the steps is described in the different Sections 19.6.4.3 to 19.6.4.7.

The idea of increasing the signal-to-noise ratio in electron images of unstained biological macromolecules by averaging was discussed in 1971 (Glaeser, 1971) and demonstrated in 1975 (Unwin & Henderson, 1975), though earlier work on stained specimens had shown the value of averaging to increase the signal-to-noise ratio. The improvement obtained, as in all repeated measurements, gives a factor of $N^{1/2}$ improvement in signal-to-noise ratio where N is the number of times the measurement is made. The effect of averaging to produce an improvement in signal-to-noise ratio is seen most clearly in the processing of images from 2D crystals. Fig. 19.6.4.2 shows the results of applying a sequence of corrections, beginning with averaging, to 2D crystals of bacteriorhodopsin in 2D space group $p3$. The panels show: (*a*, *b*) 2D averaging, (*c*) correction for the microscope contrast-transfer function (CTF), and (*d*) threefold crystallographic symmetry averaging of the phases and combination with electron-diffraction amplitudes. At each stage in the procedure the projected picture of the molecules gets clearer. The final stage results in a virtually noise-free projected structure for the molecule at atomic (3 Å) resolution.

The earliest successful application of the idea of combining projections to reconstruct the 3D structure of a biological assembly was made by DeRosier & Klug (1968). The idea is that each 2D projection corresponds after Fourier transformation to a central section of the 3D transform of the assembly. If enough independent projections are obtained, then the 3D transform will have been fully sampled and the structure can then be obtained by back-transformation of the averaged, interpolated and smoothed 3D

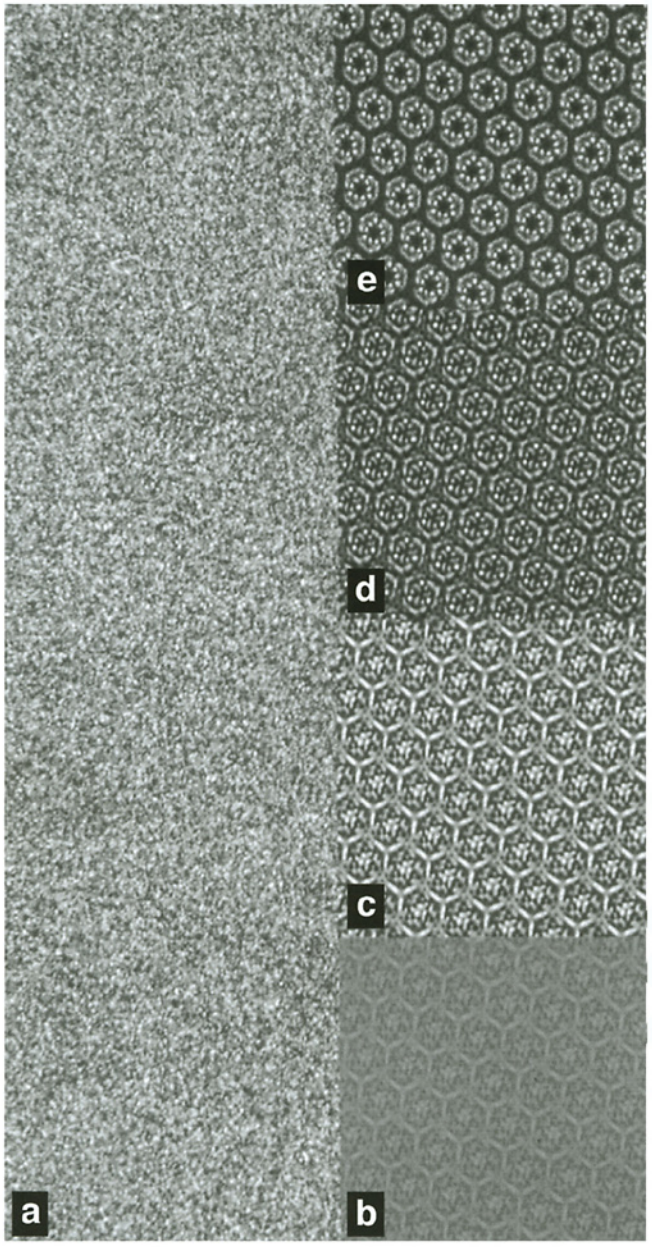

Fig. 19.6.4.2. A display of the results at different stages of image processing of a digitized micrograph of a 2D crystal of bacteriorhodopsin. The left panel (*a*) shows an area of the raw digitized micrograph in which only electron noise is visible. The lower right panel (*b*) shows the results of the averaging of unit cells from the whole picture by unbending in real space and filtering in reciprocal space. The scale of the density in (*b*) is the same as that in the original micrograph, showing that the signal is very much weaker than the noise. Panel (*c*) shows the same density as in (*b*) but with contrast increased tenfold to show that the signal in the original picture is approximately 10× below the noise level. Panel (*d*) shows the density after correction for CTF due in this case to a defocus of 6000 Å. Panel (*e*) shows the density after further threefold crystallographic averaging (the space group is *p*3 with a cell dimension of 62.5 Å) and replacement of image amplitudes by electron-diffraction amplitudes. Panel (*e*) therefore shows an almost perfect atomic resolution image of the projected structure of bacteriorhodopsin. The trimeric rings of molecules are centred on the crystallographic threefold axes and the internal structure shows α-helical segments in the protein.

transform. This procedure is shown schematically for the ubiquitous duck, which represents the molecule whose structure is being determined (Fig. 19.6.4.3).

In practice, the implementation of these concepts has been carried out in a variety of ways, since the experimental strategy and type of computer analysis used depends on the type of specimen, especially the molecular weight of the individual molecule, its symmetry and whether or not it assembles into an aggregate with one-dimensional (1D), two-dimensional (2D), or three-dimensional (3D) periodic order.

19.6.4.2. *Classification of macromolecules*

The symmetry of a macromolecule or supramolecular complex is the primary determinant of how specimen preparation, microscopy,

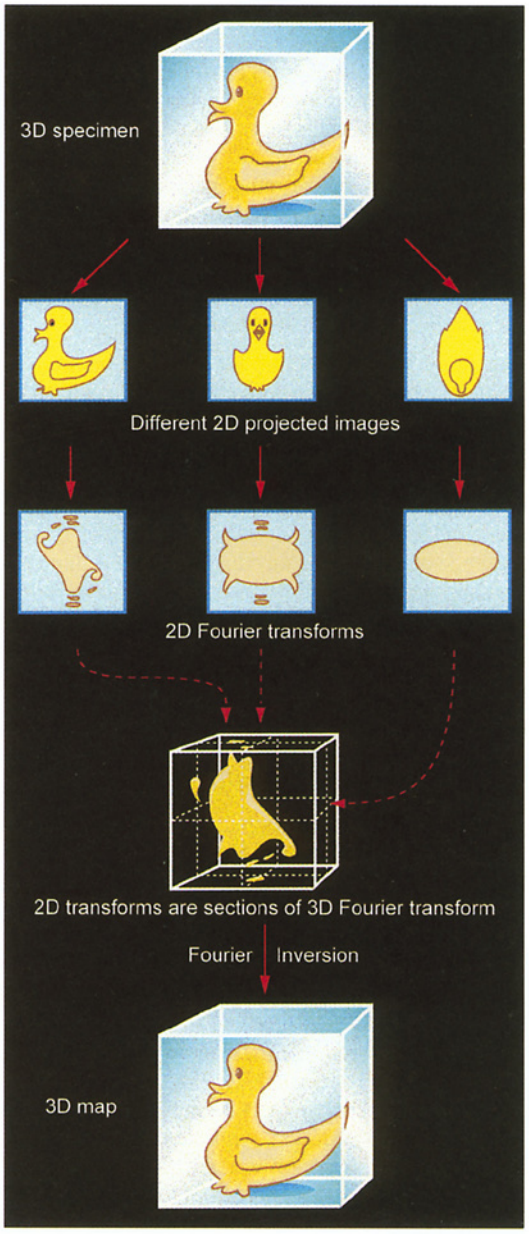

Fig. 19.6.4.3. Schematic diagram to illustrate the principle of 3D reconstruction. Each 2D projected image, as recorded on the micrograph and after CTF correction, represents a section through the 3D Fourier transform. This is called the projection theorem. After accumulation of enough information from enough different views, a 3D map of the structure can be calculated by Fourier inversion.

Table 19.6.4.1. *Classification of macromolecules according to periodic order and symmetry*

Periodic order	Type	Symmetry	Example macromolecule/complex	Representative reference
0D	Point group	C_1	Ribosome	Frank (1997)
		C_1	Centriole	Kenney *et al.* (1997)
		C_5	Bacteriophage φ29 head	Tao *et al.* (1998)
		C_8	Ribonucleoprotein vault	Kong *et al.* (1999)
		C_{17}	TMV disc	Bloomer *et al.* (1978)
		D_2	β-Galactosidase	Jacobson *et al.* (1994)
		D_6	Clathrin coats	Vigers *et al.* (1986)
		D_6	*Lumbricus terrestris* haemoglobin	de Haas *et al.* (1997)
		T	Dps protein	Grant *et al.* (1998)
		O	*Azotobacter* pyruvate dehydrogenase core	Mattevi *et al.* (1992)
		I	Icosahedral viruses	Baker *et al.* (1999)
1D	Screw axis (helical) *		Acto-myosin filament	Milligan (1996)
			Acetylcholine receptor tubes	Miyazawa *et al.* (1999)
			Microtubule	Hirose *et al.* (1997)
			Bacterial flagella	Namba & Vonderviszt (1997)
			Tobacco mosaic virus	Jeng *et al.* (1989)
2D	2D space group (2D crystal)	$p3$	Bacteriorhodopsin membrane	Henderson *et al.* (1990)
		$p42_12$	Aquaporin membrane	Cheng *et al.* (1997)
		$p6$	Gap junction membrane	Unger *et al.* (1999)
		$p321$	Light-harvesting complex II	Kühlbrandt *et al.* (1994)
		$p12_1$	Tubulin sheet	Nogales *et al.* (1998)
3D	3D space group (3D crystal)	$P2_12_12_1$	Myosin S1 protein crystal	Winkelmann *et al.* (1991)
		$P6_5$ or $P6_4$	Insect flight muscle	Taylor *et al.* (1997)

* The symmetry of a helical structure is defined by an n_m screw axis, which combines a rotation of $2\pi/n$ radians about an axis followed by a translation of m/n of the repeat distance. Because many helical structures are polymorphic, a different n_m symmetry is needed to specify each polymorph. This designation can also be confusing: for example, for tobacco mosaic virus $n_m = 16.33_{0.333}$, because the helical translational repeat consists of 49 subunits in three turns of the basic helix.

and 3D image reconstruction are performed (Sections 19.6.4.4–19.6.4.6). The classification of molecules according to their level of periodic order and symmetry (Table 19.6.4.1) provides a logical and convenient way to consider the means by which specimens are studied in 3D by microscopy.

Each type of specimen offers a unique set of challenges in obtaining 3D structural information at the highest possible resolution. The best resolutions achieved by 3D EM methods to date, at about 3–4 Å, have been obtained with several thin 2D crystals (Henderson *et al.*, 1990; Kühlbrandt *et al.*, 1994; Nogales *et al.*, 1998). These milestones have been achieved, in part, as a consequence of the excellent crystalline order exhibited by these specimens, but they are also attributable to dedicated efforts aimed at developing and refining a series of quantitative imaging and image-processing protocols, many of which are rooted in the principles and practice of Fourier-based methods used in X-ray crystallography.

With the exception of true 3D crystals, which must be sectioned to render them amenable (*i.e.* thin enough) to study by transmission electron microscopy, the resolutions obtained with biological specimens are generally dictated by the preservation of periodic order, and the symmetry and complexity of the object. Hence, studies of the helical acetylcholine receptor tubes (Miyazawa *et al.*, 1999), the icosahedral hepatitis B virus capsid (Böttcher, Wynne & Crowther, 1997), the 70S ribosome (Gabashvili *et al.*, 2000) and the centriole (Kenney *et al.*, 1997) have yielded 3D density maps at resolutions of 4.6, 7.4, 11.5 and 280 Å, respectively.

If high resolution were the sole objective of EM, it would be necessary, given the capabilities of existing technology, to try to form well ordered 2D crystals or helical assemblies of each macromolecule of interest. Indeed, a number of different crystallization techniques have been devised (*e.g.* Horne & Pasquali-Ronchetti, 1974; Yoshimura *et al.*, 1990; Kornberg & Darst, 1991; Jap *et al.*, 1992; Kubalek *et al.*, 1994; Rigaud *et al.*, 1997; Hasler *et al.*, 1998; Reviakine *et al.*, 1998; Wilson-Kubalek *et al.*, 1998) and some of these have yielded new structural information about otherwise recalcitrant molecules like RNA polymerase (Polyakov *et al.*, 1998). However, despite the obvious technological advantages of having a molecule present in a highly ordered form, most macromolecules function not as highly ordered crystals or helices but instead as single particles (*e.g.* many enzymes) or, more likely, in concert with other macromolecules as occurs in supramolecular assemblies. Also, crystallization tends to constrain the number of conformational states a molecule can adopt and the crystal conformation might not be functionally relevant. Hence, though resolution may be restricted to much below that realized in the bulk of current X-ray crystallographic studies, cryo EM methods provide a powerful means to study molecules that resist crystallization in 1D, 2D or 3D. These methods allow one to explore the dynamic events, different conformational states (as induced, for example, by altering the microenvironment of the specimen) and macromolecular interactions that are the key to understanding how each macromolecule functions.

19.6.4.3. *Specimen preparation*

The goal in preparing specimens for cryomicroscopy is to keep the biological sample as close as possible to its native state in order to preserve the structure to atomic or near atomic resolution in the

microscope and during microscopy. The methods by which numerous types of macromolecules and macromolecular complexes have been prepared for cryo EM studies are now well established (*e.g.* Dubochet *et al.*, 1988). Most such methods involve cooling samples at a rate fast enough to permit vitrification (to a solid glass-like state) rather than crystallization of the bulk water. Noncrystalline biological macromolecules are typically vitrified by applying a small (often <10 µl) aliquot of a purified ~0.2–5 mg ml^{-1} suspension of sample to an EM grid coated with a carbon or holey carbon support film. The grid, secured with a pair of forceps and suspended over a container of ethane or propane cryogen slush (maintained near its freezing point by a reservoir of liquid nitrogen), is blotted nearly dry with a piece of filter paper. The grid is then plunged into the cryogen, and the sample, if thin enough (~0.2 µm or less), is vitrified in millisecond or shorter time periods (Mayer & Astl, 1992; Berriman & Unwin, 1994; White *et al.*, 1998).

The ability to freeze samples with a timescale of milliseconds affords cryo EM one of its unique and, as yet, perhaps most under-utilized advantages: capturing and visualizing dynamic structural events that occur over time periods of a few milliseconds or longer. Several devices that allow samples to be perturbed in a variety of ways as they are plunged into a cryogen have been described (*e.g.* Subramaniam *et al.*, 1993; Berriman & Unwin, 1994; Siegel *et al.*, 1994; Trachtenberg, 1998; White *et al.*, 1998). Examples of the use of such devices include spraying acetylcholine onto its receptor to cause the receptor channel to open (Unwin, 1995), lowering the pH of an enveloped virus sample to initiate early events of viral fusion (Fuller *et al.*, 1995), inducing a temperature jump with a flash-tube system to study phase transitions in liposomes (Siegel & Epand, 1997), or mixing myosin S1 fragments with F-actin to examine the geometry of the crossbridge powerstroke in muscle (Walker *et al.*, 1999).

Crystalline (2D) samples can fortunately often be prepared for cryo EM by means of simpler procedures, and vitrification of the bulk water is not always essential to achieve success (Cyrklaff & Kühlbrandt, 1994). Such specimens may be applied to the carbon film on an EM grid by normal adhesion methods, washed with 1–2% solutions of solutes like glucose, trehalose, or tannic acid, wicked with filter paper to remove excess solution, air dried, loaded into a cold holder (see below), inserted into the microscope, and, finally, cooled to liquid-nitrogen temperature.

Specimen preparation for cryomicroscopy is, of course, easier to describe than perform ('the Devil is in the details'). Success or failure depends critically on many factors such as: sample properties (pI, presence of lipids *etc.*); sample concentration (usually much higher than that needed for negative staining) and temperature; stability, age and wetting properties of the support film and need for glow-discharging (Dubochet, Groom & Müller-Neuteboom, 1982) or use of lipids (Vénien-Bryan & Fuller, 1994) to render the film hydrophilic or hydrophobic; time of sample adsorption to the film; humidity near the sample; extent of blotting and time elapsed before freeze-plunging; and concentrations and types of solutes present in the aqueous sample or the need to remove them (Trinick & Cooper, 1990; Vénien-Bryan & Fuller, 1994). Lastly, the experience and persistence of the microscopist may be critical in judging which factors are most important. Fortunately, cryo EM has evolved long enough to demonstrate that a wide variety of fragile macromolecular assemblies can be preserved and imaged in a near-native state.

Alternative procedures exist for each step of sample preparation. Particulate specimens (*i.e.* single particles) are usually prepared on holey carbon films, which are sometimes glow-discharged to enhance the spreading of the specimen. Continuous carbon films, carbon-coated plastic films and even bare grids (Adrian *et al.*, 1984) have been used as supports for different specimens. Several techniques and freezing devices have been developed for producing uniformly thin, vitrified samples (*e.g.* Taylor & Glaeser, 1976; Dubochet, Chang *et al.*, 1982; Bellare *et al.*, 1988; Dubochet *et al.*, 1988; Trinick & Cooper, 1990). All subsequent steps, up to and including the recording of images in the microscope (Section 19.6.4.4), are carried out in a manner that maintains the sample below −170 °C to avoid devitrification, which occurs at ~−140 °C and leads to recrystallization of the bulk water to form cubic ice (Dubochet, Lepault *et al.*, 1982; Lepault *et al.*, 1983).

These steps include transfer of the grid from the cryogen into liquid nitrogen, where it may be stored indefinitely, and then into a cryo specimen holder that is cooled with liquid nitrogen (*e.g.* Dubochet *et al.*, 1988). The cold holder is rapidly but carefully inserted into the electron microscope to minimize condensation of water vapour onto the cold holder tip, otherwise such water ruins the high vacuum of the microscope and also contaminates the specimen. Indeed, because the cold specimen itself is an efficient trap for any contaminant, most cryo EM is performed on microscopes equipped with blade-type anticontaminators (*e.g.* Homo *et al.*, 1984) that permit individual EM grids to be viewed for periods of up to several hours. Also, cryo holders are subject to greater instabilities than conventional, room-temperature holders owing to the temperature gradient between microscope and specimen and because boiling of the liquid-nitrogen coolant in the Dewar of the cold holder transmits vibrations to the specimen. The maximum instrumental resolving power of most modern microscopes (~0.7–2 Å) cannot yet be realized with commercially available cold holders, which promise stability in the 2–4 Å range.

19.6.4.4. *Microscopy*

Once the vitrified specimen is inserted into the microscope and sufficient time is allowed (~15 min) for the specimen stage to stabilize to minimize drift and vibration, microscopy is performed to generate a set of images that, with suitable processing procedures, can later be used to produce a reliable 3D reconstruction of the specimen at the highest possible resolution. To achieve this goal, imaging must be performed at an electron dose that minimizes beam-induced radiation damage to the specimen, with the objective lens of the microscope defocused to enhance phase contrast from the weakly scattering, unstained biological specimen, and under conditions that keep the specimen below the devitrification temperature and minimize its contamination.

The microscopist locates specimen areas suitable for photography by searching the EM grid at very low magnification ($\leq 3000\times$) to keep the irradiation level very low (< 0.05 e $Å^{-2} s^{-1}$) while assessing sample quality: Is it vitrified and is the thickness optimal? Are the concentration and distribution of particles or is the size of the 2D crystal optimal? In microscopes operated at 200 keV or higher, where image contrast is very weak, it is helpful to perform the search procedure with the assistance of a CCD camera or a video-rate TV-intensified camera system. CCD cameras are gaining popularity because imaging conditions (defocus level, astigmatism, specimen drift or vibration *etc.*) can be accurately monitored and adjusted by computing the image Fourier transform online (Sherman *et al.*, 1996) and also because in some cases the distribution of single particles can be seen at low or moderate magnifications (Olson *et al.*, 1997). For some specimens, like thin 2D crystals, searching is conveniently performed by viewing the low-magnification high-contrast image produced by slightly defocusing the electron-diffraction pattern using the diffraction lens.

After a desired specimen area is identified, the microscope is switched to high-magnification mode for focusing and astigmatism correction. These adjustments are typically performed in a region ~2–10 µm away from the chosen area at the same or higher magnification than that used for photography. The choice of

magnification, defocus level, accelerating voltage, beam coherence, electron dose and other operating conditions is dictated by several factors. The most significant ones are the size of the particle or crystal unit cell being studied, the anticipated resolution of the images and the requirements of the image processing needed to compute a 3D reconstruction to the desired resolution. For most specimens at required resolutions from 3 to 30 Å, images are typically recorded at 25000–50000× magnification with an electron dose of between 5 and 20 e Å^{-2}. Even lower magnification, down to 10000×, can be used if high resolution is not required, and higher magnification, up to 75000×, can be used if good specimen areas are easy to locate. These conditions yield micrographs of sufficient optical density (OD 0.2–1.5) and image resolution for subsequent image processing steps (Sections 19.6.4.5 and 19.6.4.6). Most modern EMs provide some mode of low-dose operation for imaging beam-sensitive, vitrified biological specimens. Dose levels may be measured directly (*e.g.* with a Faraday cup) or they may be estimated from a calibrated microscope exposure meter (*e.g.* Baker & Amos, 1978).

The intrinsic low contrast of unstained specimens makes it impossible to observe and focus on specimen details directly as is routine with stained or metal-shadowed specimens. Focusing, aimed to enhance phase contrast in the recorded images but minimize beam damage to the desired area, is achieved by judicious defocusing on a region that is adjacent to the region to be photographed and preferably situated on the microscope tilt axis. The appropriate focus level is set by adjusting the appearance of either the Fresnel fringes that occur at the edges of holes in the carbon film or the 'phase granularity' from the carbon support film (*e.g.* Agar *et al.*, 1974).

Unfortunately, electron images do not give a direct rendering of the specimen density distribution. The relationship between image and specimen is described by the contrast-transfer function (CTF) which is characteristic of the particular microscope used, the specimen and the conditions of imaging. The microscope CTF arises from the objective-lens focal setting and from the spherical aberration present in all electromagnetic lenses, and varies with the defocus and accelerating voltage according to equation (19.6.4.1), an expression which includes both phase and amplitude contrast components. First, however, it might be useful to describe briefly the essentials of amplitude contrast and phase contrast, two concepts carried over from optical microscopy. Amplitude contrast refers to the nature of the contrast in an image of an object which absorbs the incident illumination or scatters it in any other way so that a proportion of it is lost. As a result, the image appears darker where greater absorption occurs. Phase contrast is required if an object is transparent (*i.e.* it is a pure phase object) and does not absorb but only scatters the incident illumination. Biological specimens for cryo EM are almost pure phase objects and the scattering is relatively weak, so the simple theory of image formation by a weak phase object applies (Spence, 1988; Reimer, 1989). An exactly in-focus image of a phase object has no contrast variation since all the scattered illumination is focused back to equivalent points in the image of the object from which it was scattered. In optical microscopy, the use of a quarter wave plate can retard the phase of the direct unscattered beam, so that an in-focus image of a phase object has very high 'Zernicke' phase contrast. However, there is no simple quarter wave plate for electrons, so instead phase contrast is created by introducing phase shifts into the diffracted beams by adjustment of the excitation of the objective lens so that the image is slightly defocused. In addition, since all matter is composed of atoms and the electric potential inside each atom is very high near the nucleus, even the electron-scattering behaviour of the light atoms found in biological molecules deviates from that of a weak phase object, but for a deeper discussion of this the reader should refer to Reimer (1989) or Spence (1988). In practice, the proportion of 'amplitude' contrast is about 7% at 100 kV and 5% at 200 kV for low-dose images of protein molecules embedded in ice.

The overall dependence of the CTF on resolution, wavelength, defocus and spherical aberration is

$$\mathrm{CTF}(\nu) = -\left\{\left(1 - F_{\mathrm{amp}}^2\right)^{1/2} \sin[\chi(\nu)] + F_{\mathrm{amp}} \cos[\chi(\nu)]\right\}, \tag{19.6.4.1}$$

where $\chi(\nu) = \pi\lambda\nu^2(\Delta f - 0.5C_s\lambda^2\nu^2)$, ν is the spatial frequency (in Å^{-1}), F_{amp} is the fraction of amplitude contrast, λ is the electron wavelength (in Å), where $\lambda = 12.3/(V + 0.000000978V^2)^{1/2}$ (= 0.037, 0.025 and 0.020 Å for 100, 200 and 300 keV electrons, respectively), V is the voltage (in volts), Δf is the underfocus (in Å) and C_s is the spherical aberration of the objective lens of the microscope (in Å).

In addition, this CTF is attenuated by an envelope or damping function which depends upon the spatial and temporal coherence of the beam, specimen drift and other factors (Erickson & Klug, 1971; Frank, 1973; Wade & Frank, 1977; Wade, 1992). Fig. 19.6.4.4 shows a few representative CTFs for different amounts of defocus on a normal and a FEG microscope. Thus, for a particular defocus setting of the objective lens, phase contrast in the electron image is positive and maximal only at a few specific spatial frequencies. Contrast is either lower than maximal, completely absent, or it is opposite (inverted or reversed) from that at other frequencies. Hence, as the objective lens is focused, the electron microscopist selectively accentuates image details of a particular size. For this discussion, we ignore inelastic scattering, which makes some limited contribution at low resolution to images as a result of the effect of chromatic aberration on the energy-loss electrons in thick specimens or samples embedded in thick layers of vitrified water (Langmore & Smith, 1992). Inelastically scattered electrons can be largely removed by use of microscopes equipped with electron-energy filtering devices (*e.g.* Langmore & Smith, 1992; Koster *et al.*, 1997; Zhu *et al.*, 1997), but this also leaves fewer electrons to form the image.

Images are typically recorded 0.8–3.0 µm underfocus to enhance specimen features in the 20–40 Å size range and thereby facilitate phase-origin and specimen-orientation search procedures carried out in the image-processing steps (Section 19.6.4.8), but this level of underfocus also enhances contrast in lower-resolution maps, which may help in interpretation. To obtain results at better than 10–15 Å resolution, it is essential to record, process and combine data from several micrographs that span a range of defocus levels (*e.g.* Unwin & Henderson, 1975; Böttcher, Wynne & Crowther, 1997). This strategy assures good information transfer at all spatial frequencies up to the limiting resolution but requires careful compensation for the effects of the microscope CTF during image processing. Also, the recording of image focal pairs or focal series from a given specimen area can be beneficial in determining origin and orientation parameters for processing of images of single particles (*e.g.* Cheng *et al.*, 1992; Trus *et al.*, 1997; Conway & Steven, 1999).

Many high-resolution cryo EM studies are now performed with microscopes operated at 200 keV or higher and with FEG electron sources (*e.g.* Zemlin, 1992; Zhou & Chiu, 1993; Zemlin, 1994; Mancini *et al.*, 1997). The high coherence of a FEG source ensures that phase contrast in the images remains strong out to high spatial frequencies ($> 1/3.5$ Å^{-1}) even for highly defocused images. The use of higher voltages provides potentially higher resolution (greater depth of field – *i.e.* less curvature of the Ewald sphere – owing to the smaller electron-beam wavelength), better beam penetration (less multiple scattering), reduced problems with specimen charging of the kind that plague microscopy of unstained

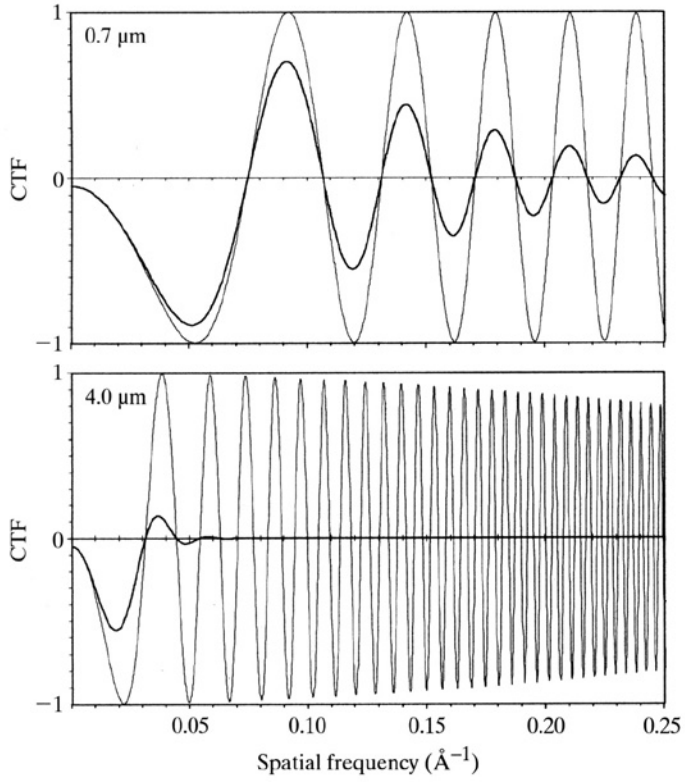

Fig. 19.6.4.4. Representative plots of the microscope contrast-transfer function (CTF) as a function of spatial frequency, for two different defocus settings (0.7 and 4.0 μm underfocus) and for a field-emission (light curve) or tungsten (dark curve) electron source. All plots correspond to electron images formed in an electron microscope operated at 200 kV with objective-lens aberration coefficients $C_s = C_c = 2.0$ mm and assuming amplitude contrast of 4.8% (Toyoshima *et al.*, 1993). The spatial coherence, which is related to the electron source size and expressed as β, the half-angle of illumination, for tungsten and FEG electron sources was fixed at 0.3 and 0.015 mrad, respectively. Likewise, the temporal coherence (expressed as ΔE, the energy spread) was fixed at 1.6 and 0.5 eV for tungsten and FEG sources. The combined effects of the poorer spatial and temporal coherence of the tungsten source leads to a significant dampening, and hence loss of contrast, of the CTF at progressively higher resolutions compared to that observed in FEG-equipped microscopes. The greater number of contrast reversals with higher defocus arises because of the greater out-of-focus phase shifts as described in Section 19.6.4.4.

or uncoated vitrified specimens (Brink *et al.*, 1998) and reduced phase shifts associated with beam tilt.

Images are recorded on photographic film or on a CCD camera with either flood-beam or spot-scan procedures. Film, with its advantages of low cost, large field of view and high resolution (~10 μm), has remained the primary image-recording medium for most cryo EM applications, despite disadvantages of high background fog and need for chemical development and digitization. CCD cameras provide image data directly in digital form and with very low background noise, but suffer from higher cost, limited field of view, limited spatial resolution caused by poor point spread characteristics and a fixed pixel size (24 μm). They are useful, for example, for precise focusing and adjustment of astigmatism (*e.g.* Krivanek & Mooney, 1993; Sherman *et al.*, 1996). With conventional flood-beam imaging, the electron beam (generally >2–5 μm diameter) illuminates an area of specimen that exceeds what is recorded in the micrograph. In spot-scan imaging, which decreases the beam-induced specimen drift often seen in flood illumination, a 2000 Å or smaller diameter beam is scanned across the specimen in a square or hexagonal pattern while the image is recorded (Downing, 1991). This method is beneficial in the examination of 2D crystalline specimens at near-atomic resolutions (Henderson *et al.*, 1990; Nogales *et al.*, 1998) and has also been used to study some icosahedral viruses (*e.g.* Zhou *et al.*, 1994; Zhao *et al.*, 1995).

For studies in which specimens must be tilted to collect 3D data, such as with 2D crystals, single particles that adopt preferred orientations on the EM grid, or specimens requiring tomography, microscopy is performed in essentially the same way as described above. However, the limited tilt range (±60–70°) of most microscope goniometers can lead to non-isotropic resolution in the 3D reconstructions (the 'missing cone' problem), and tilting generates a constantly varying defocus across the field of view in a direction normal to the tilt axis. The effects caused by this varying defocus level must be corrected in high-resolution applications (Henderson *et al.*, 1990) or they can be partially corrected during spot-scan microscopy if the defocus of the objective lens is varied in proportion to the distance between the beam and tilt axis (Zemlin, 1989).

19.6.4.5. *Selection and preprocessing of digitized images*

Before any image analysis or classification of the molecular images can be done, a certain amount of preliminary checking and normalization is required to ensure there is a reasonable chance that a homogeneous population of molecular images has been obtained. First, good-quality micrographs are selected in which the electron exposure is correct, there is no image drift or blurring, and there is minimal astigmatism and a reasonable amount of defocus to produce good phase contrast. This is usually done by visual examination and optical diffraction.

Once the best pictures have been chosen, the micrographs must be scanned and digitized on a suitable densitometer. The sizes of the steps between digitization of optical density, and the size of the sample aperture over which the optical density is averaged by the densitometer, must be sufficiently small to sample the detail present in the image at fine enough intervals (DeRosier & Moore, 1970). Normally, a circular (or square) sample aperture of diameter (or length of side) equal to the step between digitization is used. This avoids digitizing overlapping points, without missing any of the information recorded in the image. The size of the sample aperture and digitization step depends on the magnification selected and the resolution required. A value of one-quarter to one-third of the required limit of resolution (measured in μm on the emulsion) is normally ideal, since it avoids having too many numbers (and therefore wasting computer resources) without losing anything during the measurement procedure. For a 40000× image, on which a resolution of 10 Å at the specimen is required, a step size of 10 μm [= (1/4)(10 Å × 40000/10000 Å μm^{-1})] would be suitable.

The best area of an image of a helical or 2D crystal specimen can then be boxed off using a soft-edged mask. For images of single particles, a stack of individual particles can be created by selecting out many small areas surrounding each particle. In the later steps of image processing, because the orientation and position of each particle are refined by comparing the amplitudes and phases of their Fourier components, it is important to remove spurious features around the edge of each particle and to make sure the different particle images are on the same scale. This is normally done by masking off a circular area centred on each particle and floating the density so that the average around the perimeter becomes zero (DeRosier & Moore, 1970). The edge of the mask is apodized, which means the application of a soft cosine bell shape to the original densities so they taper towards the background level. Finally, to compensate for variations in the exposure due to ice thickness or electron dose, most workers normalize the stack of

individual particle images so that the mean density and mean density variation over the field of view are set to the same values for all particles (Carrascosa & Steven, 1978).

Once some good particles or crystalline areas for 1D or 2D crystals have been selected, digitized and masked and their intensity values have been normalized, true image processing can begin.

19.6.4.6. *Image processing and 3D reconstruction*

Although the general concepts of signal averaging, together with combining different views to reconstruct the 3D structure, are common to the different computer-based procedures which have been implemented, it is important to emphasize one or two preliminary points. First, a homogeneous set of particles must be selected for inclusion in the 3D reconstruction. This selection may be made by eye to eliminate obviously damaged particles or impurities, or by the use of multivariate statistical analysis (van Heel & Frank, 1981) or some other classification scheme. This allows a subset of the particle images to be used to determine the structure of a better-defined entity. All image-processing procedures require the determination of the same parameters that are needed to specify unambiguously how to combine the information from each micrograph or particle. These parameters are: the magnification, defocus, astigmatism and, at high resolution, the beam tilt for each micrograph; the electron wavelength used (*i.e.* accelerating voltage of the microscope); the spherical aberration coefficient, C_s, of the objective lens; and the orientation and phase origin for each particle or unit cell of the 1D, 2D or 3D crystal. There are 13 parameters for each particle, eight of which may be common to each micrograph and two or three (C_s, accelerating voltage, magnification) to each microscope. The different general approaches that have been used in practice to determine the 3D structure of different classes of macromolecular assemblies from one or more electron micrographs are listed in Table 19.6.4.2.

The precise way in which each general approach codes and determines the particle or unit-cell parameters varies greatly and is not described in detail. Much of the computer software used in image-reconstruction studies is relatively specialized compared with that used in the more mature field of macromolecular X-ray crystallography. In part, this may be attributed to the large diversity of specimen types amenable to cryo EM and reconstruction methods. As a consequence, image-reconstruction software is evolving quite rapidly, and references to software packages cited in Table 19.6.4.2 are likely to become quickly outdated. Extensive discussion of algorithms and software packages in use at this time may be found in a number of recent special issues of *Journal of Structural Biology* (Vol. 116, No. 1; Vol. 120, No. 3; Vol. 121, No. 2; Vol. 125, Nos. 2–3).

In practice, attempts to determine or refine some parameters may be affected by the inability to determine accurately one of the other parameters. The solution of the structure is therefore an iterative procedure in which reliable knowledge of the parameters that describe each image is gradually built up to produce a more and more accurate structure until no more information can be squeezed out of the micrographs. At this point, if any of the origins or orientations are wrongly assigned, there will be a loss of detail and a decrease in signal-to-noise ratio in the map. If a better-determined or higher-resolution structure is required, it would then be necessary to record images on a better microscope or to prepare new specimens and record better pictures.

The reliability and resolution of the final reconstruction can be measured using a variety of indices. For example, the differential phase residual (DPR) (Frank *et al.*, 1981), the Fourier shell correlation (FSC) (van Heel, 1987*b*) and the Q factor (van Heel & Hollenberg, 1980) are three such measures. The DPR is the mean phase difference, as a function of resolution, between the structure factors from two independent reconstructions, often calculated by splitting the image data into two halves. The FSC is a similar calculation of the mean correlation coefficient between the complex structure factors of the two halves of the data as a function of resolution. The Q factor is the mean ratio of the vector sum of the individual structure factors from each image divided by the sum of their moduli, again calculated as a function of resolution. Perfectly accurate measurements would have values of the DPR, FSC and Q factor of 0°, 1.0 and 1.0, respectively, whereas random data containing no information would have values of 90°, 0.0 and 0.0. The spectral signal-to-noise ratio (SSNR) criterion has been advocated as the best of all (Unser *et al.*, 1989): it effectively measures, as a function of resolution, the overall signal-to-noise ratio (squared) of the whole of the image data. It is calculated by taking into consideration how well all the contributing image data agree internally.

An example of a strategy for determination of the 3D structure of a new and unknown molecule without any symmetry and which does not crystallize might be as follows:

(1) Record a single-axis tilt series of particles embedded in negative stain, with a tilt range from −60° to +60°.

(2) Calculate 3D structures for each particle using an R-weighted back-projection algorithm (Radermacher, 1992).

(3) Average 3D data for several particles in real or reciprocal space to get a reasonably good 3D model of the stain-excluding region of the particle.

(4) Record a number of micrographs of the particles embedded in vitreous ice.

(5) Use the 3D negative-stain model obtained in (3) with inverted contrast to determine the rough alignment parameters of the particle in the ice images.

(6) Calculate a preliminary 3D model of the average ice-embedded structure.

(7) Use the preliminary 3D model to determine more accurate alignment parameters for the particles in the ice images.

(8) Calculate a better 3D model.

(9) Determine defocus and astigmatism to allow CTF calculation and correct 3D model so that it represents the structure at high resolution.

(10) Keep adding pictures at different defocus levels to get an accurate structure at as high a resolution as possible.

For large single particles with no symmetry, particles with higher symmetry or crystalline arrays, it is usually possible to miss out the negative-staining steps and go straight to alignment of particle images from ice embedding, because the particle or crystal tilt angles can be determined internally from comparison of phases along common lines in reciprocal space or from the lattice or helix parameters from a 2D or 1D crystal.

The following discussion briefly outlines for a few specific classes of macromolecule the general strategy for carrying out image processing and 3D reconstruction.

19.6.4.6.1. *2D crystals*

For 2D crystals, the general 3D reconstruction approach consists of the following steps. First, a series of micrographs of single 2D crystals are recorded at different tilt angles, with random azimuthal orientations. Each crystal is then unbent using cross-correlation techniques to identify the precise position of each unit cell (Henderson *et al.*, 1986), and amplitudes and phases of the Fourier components of the average of that particular view of the structure are obtained for the transform of the unbent crystal. The reference image used in the cross-correlation calculation can either be a part of the whole image masked off after a preliminary round of

Table 19.6.4.2. *Methods of three-dimensional image reconstruction*

Structure type (symmetry)	Method	Reference(s) to technical/theoretical details
Asymmetric (point group C_1)	Random conical tilt	Radermacher *et al.* (1987); Radermacher (1988); Frank (1996)
	Software package	Frank *et al.* (1996)
	Angular reconstitution	van Heel (1987*a*); Schatz *et al.* (1995)
	Software package	van Heel *et al.* (1996)
	Weighted back-projection	Radermacher (1991, 1992)
	Radon transform alignment	Radermacher (1994)
	Reference-based alignment	Penczek *et al.* (1994)
	Reference-free alignment	Schatz & van Heel (1990); Penczek *et al.* (1992)
	Fourier reconstruction and alignment	Grigorieff (1998)
	Tomographic tilt series and remote control of microscope *	Olins *et al.* (1983); Skoglund & Daneholt (1986); Fung *et al.* (1996); Baumeister *et al.* (1999)
Symmetric (point groups C_n, D_n; $n > 1$)	Angular reconstitution	van Heel (1987*a*); Schatz *et al.* (1995)
	Software packages	van Heel *et al.* (1996); Shah & Stewart (1998)
	Fourier–Bessel synthesis	Tao *et al.* (1998)
	Reference-based alignment and weighted back-projection	Beuron *et al.* (1998)
Icosahedral (point group I)	Fourier–Bessel synthesis (common lines)	Crowther *et al.* (1970); Crowther (1971); Fuller *et al.* (1996); Mancini *et al.* (1997)
	Reference-based alignment	Cheng *et al.* (1994); Crowther *et al.* (1994); Baker & Cheng (1996); Castón *et al.* (1999); Conway & Steven (1999)
	Software packages	Crowther *et al.* (1996); Lawton & Prasad (1996); Thuman-Commike & Chiu (1996); Boier Martin *et al.* (1997); Zhou, Chiu *et al.* (1998)
	Angular reconsitution	van Heel (1987*a*); Stewart *et al.* (1997)
	Tomographic tilt series	Walz *et al.* (1997)
Helical	Fourier–Bessel synthesis	DeRosier & Klug (1968); DeRosier & Moore (1970); Stewart (1988); Toyoshima & Unwin (1990); Morgan & DeRosier (1992); Unwin (1993); Beroukhim & Unwin (1997); Miyazawa *et al.* (1999)
	Software packages and filament straightening routines	Egelman (1986); Carragher *et al.* (1996); Crowther *et al.* (1996); Owen *et al.* (1996); Beroukhim & Unwin (1997)
2D crystal	Random azimuthal tilt	Henderson & Unwin (1975); Amos *et al.* (1982); Henderson *et al.* (1986); Baldwin *et al.* (1988); Henderson *et al.* (1990)
	Software packages	Crowther *et al.* (1996); Hardt *et al.* (1996)
3D crystal	Oblique section reconstruction	Crowther & Luther (1984); Taylor *et al.* (1997)
	Software package	Winkler & Taylor (1996)
	Sectioned 3D crystal	Winkelmann *et al.* (1991)

* Electron tomography is the subject of an entire issue of *Journal of Structural Biology* [(1997), **120**, pp. 207–395] and a book edited by Frank (1992).

averaging by reciprocal-space filtering of the regions surrounding the diffraction spots in the transform, or it can be a reference image calculated from a previously determined 3D model. The amplitudes and phases from each image are then corrected for the CTF and beam tilt (Henderson *et al.*, 1986, 1990; Havelka *et al.*, 1995) and merged with data from many other crystals by scaling and origin refinement, taking into account the proper symmetry of the 2D space group of the crystal. Finally, the whole data set is fitted by least squares to constrained amplitudes and phases along the lattice lines (Agard, 1983) prior to calculating a map of the structure. The initial determination of the 2D space group can be carried out by a statistical test of the phase relationships in one or two images of untilted specimens (Valpuesta *et al.*, 1994). The absolute hand of the structure is automatically correct since the 3D structure is calculated from images whose tilt axes and tilt angle are known. Nevertheless, care must be taken not to make any of a number of trivial mistakes that would invert the hand.

19.6.4.6.2. *Helical particles*

The basic steps involved in processing and 3D reconstruction of helical specimens include: Record a series of micrographs of vitrified particles suspended over holes in a perforated carbon support film. The micrographs are digitized and Fourier transformed to determine image quality (astigmatism, drift, defocus, presence and quality of layer lines, *etc.*). Individual particle images are boxed, floated, and apodized within a rectangular mask. The parameters of helical symmetry (number of subunits per turn and

pitch) must be determined by indexing the computed diffraction patterns. If necessary, simple spline-fitting procedures may be employed to 'straighten' images of curved particles (Egelman, 1986), and the image data may be reinterpolated (Owen *et al.*, 1996) to provide more precise sampling of the layer-line data in the computed transform. Once a preliminary 3D structure is available, a much more sophisticated refinement of all the helical parameters can be used to unbend the helices on to a predetermined average helix so that the contributions of all parts of the image are correctly treated (Beroukhim & Unwin, 1997). The layer-line data are extracted from each particle transform and two phase origin corrections are made: one to shift the phase origin to the helix axis (at the centre of the particle image) and the other to correct for effects caused by having the helix axis tilted out of the plane normal to the electron beam in the electron microscope. The layer-line data are separated out into near- and far-side data, corresponding to contributions from the near and far sides of each particle imaged. The relative rotations and translations needed to align the different transforms are determined so the data may be merged and a 3D reconstruction computed by Fourier–Bessel inversion procedures (DeRosier & Moore, 1970).

19.6.4.6.3. *Icosahedral particles*

The typical strategy for processing and 3D reconstruction of icosahedral particles consists of the following steps: First, a series of micrographs of a monodisperse distribution of particles, normally suspended over holes in a perforated carbon support film, is recorded. After digitization of the micrographs, individual particle images are boxed and floated with a circular mask. The astigmatism and defocus of each micrograph is measured from the sum of intensities of the Fourier transforms of all particle images (Zhou *et al.*, 1996). Auto-correlation techniques are then used to estimate the particle phase origins, which coincide with the centre of each particle where all rotational symmetry axes intersect (Olson & Baker, 1989). The view orientation of each particle, defined by three Eulerian angles, is determined either by means of common and cross-common lines techniques or with the aid of model-based procedures (*e.g.* Crowther, 1971; Fuller *et al.*, 1996; Baker *et al.*, 1999). Once a set of self-consistent particle images is available, an initial low-resolution 3D reconstruction is computed by merging these data with Fourier–Bessel methods (Crowther, 1971). This reconstruction then serves as a reference for refining the orientation, origin and CTF parameters of each of the included particle images, for rejecting 'bad' images, and for increasing the size of the data set by including new particle images from additional micrographs taken at different defocus levels. A new reconstruction, computed from the latest set of images, serves as a new reference and the above refinement procedure is repeated until no further improvements as measured by the reliability criteria mentioned above are made.

19.6.4.7. *Visualization, modelling and interpretation of results*

Once a reliable 3D map is obtained, computer graphics and other visualization tools may be used as aids in interpreting morphological details and understanding biological function in the context of biochemical and molecular studies and complementary X-ray crystallographic and other biophysical measurements.

Initially, for low-resolution studies (>10 Å) and where the structure is unknown, the gross shape (molecular envelope) of the macromolecule is best visualized with volume-rendering programs (*e.g.* Conway *et al.*, 1996; Sheehan *et al.*, 1996; Spencer *et al.*, 1997). Such programs establish a density threshold, above which all density is represented as a solid and below which all density is invisible (representing possible solvent regions). Choice of the threshold that accurately represents the solvent-excluded density can prove problematic, especially if the microscope CTF is uncorrected (*e.g.* Conway *et al.*, 1996). For qualitative examination of maps, a threshold at 1.5 or 2 standard deviations above the background noise level provides a practical choice. Another, semi-quantitative, approach is to adjust the threshold to produce a volume consistent with the expected total molecular mass. This procedure is prone to error because the volume is sensitive to small changes in contour level, which, in turn, is highly sensitive to scaling and CTF correction. Caution should therefore be exercised in drawing conclusions based on volume fluctuations of less than 20% of that expected. As a general guide, solid-surface rendering in the range 80 to 120% of the expected volume gives reasonable shape and connectivity.

A complete description of available graphical tools for visualizing 3D density maps is beyond the scope of this discussion, but it is worth noting several of the principles by which 3D data can be rendered. Stereo images (*e.g.* Liu *et al.*, 1994; Agrawal *et al.*, 1996; Taveau, 1996; Winkler *et al.*, 1996; Nogales *et al.*, 1997; Kolodziej *et al.*, 1998; Gabashvili *et al.*, 2000) provide a powerful way to convey the 3D structure. Also, as in X-ray crystallographic applications, stereo viewing is essential for exploring details of secondary and tertiary structural information in high-resolution 3D maps (*e.g.* Henderson *et al.*, 1990; Böttcher, Wynne & Crowther, 1997). Additional visualization tools include: use of false colour to highlight distinct components (*e.g.* Yeager *et al.*, 1994; Cheng *et al.*, 1995; Hirose *et al.*, 1997; Metoz *et al.*, 1997; Zhou *et al.*, 1999) and a variety of computer 'sectioning' or image-projection algorithms that produce cut-open views (*e.g.* Vigers *et al.*, 1986; Cheng *et al.*, 1994; Fuller *et al.*, 1995), spherical sections (*e.g.* Baker *et al.*, 1991), icosahedrally cut surfaces (Böttcher, Kiselev *et al.*, 1997), polar sections (Fuller *et al.*, 1995), cylindrical sections (*e.g.* Hirose *et al.*, 1997), radial projections (*e.g.* Dryden *et al.*, 1993), and radial depth cueing (Spencer *et al.*, 1997), which conveys an immediate, and often quantitative, view of the radial placement of details in a map (Grimes *et al.*, 1997). Animation also provides an alternative approach to enhance the viewer's perception of the 3D structure (*e.g.* van Heel *et al.*, 1996; Frank *et al.*, 1999). All these rendering methods should always be carefully described so the reader may distinguish representation from result.

Difference imaging and density-map modelling are examples of two additional techniques that can sometimes enhance interpretation of 3D cryo EM data.

Difference imaging is a very powerful tool, long employed by structural biologists outside the cryo EM field, that permits small (or large) differences among closely related structures to be examined. One of the great advantages of cryomicroscopy of ice-embedded specimens over microscopy using negative stains is that cryo EM difference imaging yields more reliable results as confirmed by correlation with biochemical and immunological data (*e.g.* Baker *et al.*, 1990; Stewart *et al.*, 1993; Vénien-Bryan & Fuller 1994; Yeager *et al.*, 1994; Hoenger & Milligan, 1997; Lawton *et al.*, 1997; Stewart *et al.*, 1997; Böttcher *et al.*, 1998; Conway *et al.*, 1998; Sharma *et al.*, 1998; Zhou, Mcnab *et al.*, 1998). However, reliable interpretation is only possible if the difference maps are carefully calculated (*i.e.* from two maps calculated to the same resolution and scaled in such a way that the differences are minimized). Subtraction of two maps, each having an intrinsic noise level, guarantees that the difference map will always be noisier than either of the parent maps, and noise in the difference map is what determines the significance of features in it. Careful statistical analysis is an important prerequisite in attributing significance to and interpreting particular features. One critical test is to see whether a difference of a similar size can be found between independent determinations of the same structure. Differences that

occur at symmetry axes must be treated cautiously, because the noise level there is greater.

The combination of X-ray and cryo EM data provides a powerful tool for interpreting structures [*e.g.* see the review by Baker & Johnson (1996)]. A high-resolution X-ray model can be docked into a cryo EM density map with greater precision than the nominal resolution of the map. Several similar protocols have been developed for fitting X-ray data to cryo EM reconstructions (*e.g.* Wikoff *et al.*, 1994; Che *et al.*, 1998; Volkmann & Hanein, 1999; Wriggers *et al.*, 1999). First, because magnification in an electron microscope can vary, the absolute magnification of the reconstruction to within a few per cent must be established. In addition, the relative scale factor for the density must be calculated. Determination of absolute magnification and relative scaling may be accomplished by several means: (1) comparing the EM map with clear features in the X-ray structure of an individual component (Stewart *et al.*, 1993), (2) using radial density profile information derived from scattering experiments (*e.g.* Cheng *et al.*, 1995), or (3) using the X-ray structure of an entire assembly when this is available (*e.g.* Speir *et al.*, 1995). When a single component is used for scaling, it is necessary to refine the scale as the proper position and orientation of that component become better determined. Next, the resolution of the density distribution of the reconstruction must be matched to that in the X-ray structure. For example, fitting of the high-resolution model of the adenovirus hexon to the EM density map of the virus itself was accomplished by convoluting the X-ray structure with the point-spread function for the EM reconstruction (Stewart *et al.*, 1993). An alternative procedure is simply to normalize the EM map so that it has the same range of density values as the corresponding X-ray map (*e.g.* Luo *et al.*, 1993; Wikoff *et al.*, 1994; Ilag *et al.*, 1995). A maximum-entropy approach (Skoglund *et al.*, 1996) was also used to treat CTF effects to improve the correspondence between the adenovirus hexon X-ray structure and the corresponding density in the EM map (Stewart *et al.*, 1993).

The next step in the modelling procedure is to fit the X-ray structure interactively to the cryo EM density using a display program such as *O* (Jones *et al.*, 1991), at which point a subjective estimate of the quality of the fit can be made. One criterion for the quality of the fit is whether the hand of the structure can be identified. Because 3D density maps are generated from projected views of the structure, an arbitrary hand will emerge during refinement unless explicit steps are taken to determine the absolute hand. Thus, in the absence of relatively high resolution data (which, for example, would reveal the hand of features like α-helices), the absolute hand must be determined from other types of data such as shadowing (*e.g.* Belnap *et al.*, 1996) or comparison of the orientations of the same particle imaged at different tilt angles (*e.g.* Finch, 1972; Belnap *et al.*, 1997). The match with X-ray data (of known hand) serves as an unambiguous determination of hand for the EM map. At this stage of fitting it is important to determine whether the X-ray model should be fitted as a single rigid body (*e.g.* Stewart *et al.*, 1993) or as two or more partly independent domains (*e.g.* Grimes *et al.*, 1997; Che *et al.*, 1998; Volkmann & Hanein, 1999).

The quality and uniqueness of the X-ray/EM map fit is then assessed, often simply by calculating an *R* factor between the two maps. It may be necessary first to mask out density that is not part of the structure being fitted by the X-ray data (*e.g.* Stewart *et al.*, 1993; Liu *et al.*, 1994; Cheng *et al.*, 1995). The uniqueness of the fit is then tested by rotating and shifting the X-ray model in the EM map and noting changes in the *R* factor (*e.g.* Che *et al.*, 1998). An objective fitting procedure, either in reciprocal or real space, is necessary for refining and checking the uniqueness of the result of the interactive fitting. The program *X-PLOR* (Brünger *et al.*, 1987) can be used for reciprocal-space refinement after the two maps are modified to avoid ripple and edge effects due to masking and differences in contrast (*e.g.* Wikoff *et al.*, 1994; Grimes *et al.*, 1997; Hewat *et al.*, 1997). Real-space refinement has been performed using other programs (*e.g.* Volkmann & Hanein, 1999; Wriggers *et al.*, 1999). A few examples include fitting the Sindbis capsid protein to the Ross River virion map (Cheng *et al.*, 1995), fitting the VP7 viral protein into the bluetongue virus core map (Grimes *et al.*, 1997), fitting the Ncd motor domain to microtubules (Wriggers *et al.*, 1999), and fitting of two separate macromolecules, the myosin S1 subfragment and the N-terminal domain of human T-fimbrin, to reconstructions of complexes between these molecules and actin filaments (Volkmann & Hanein, 1999). Comparison between results of real- and reciprocal-space fitting can prove informative. For example, reciprocal-space fitting is usually not constrained to avoid interpenetration of the densities, an issue more easily addressed in real-space fitting. If the two approaches yield different fits, it may be necessary to consider conformation changes between the X-ray and the EM structure. This type of analysis is best performed with quantitative model-fitting routines such as those currently being developed (*e.g.* Volkmann & Hanein, 1999; Wriggers *et al.*, 1999).

19.6.4.8. *Solving the X-ray phase problem with cryo EM maps*

Correlation of EM and X-ray data is not limited to situations in which a high-resolution structure from X-ray diffraction is used to enhance the interpretation of an EM reconstruction. For example, in several virus crystallography studies, an EM map was used to help solve the phase problem in the solution of the X-ray structure. This approach has the advantage in that it avoids the need for heavy-atom derivatives, which produce only small changes in the scattering of a large object such as a virus and also often introduce problems of non-isomorphism. The first such example was the determination of the structure of cowpea chlorotic mottle virus (CCMV), in which an EM reconstruction was used to construct an initial model for phasing the X-ray data (Speir *et al.*, 1995). The atomic coordinates of southern bean mosaic virus were placed into the CCMV EM density map, and a rotation function was calculated to 15 Å and used to orient the model with respect to the crystallographic data. Phases were calculated from the oriented model and then extended to 4 Å by the use of standard phase-extension and noncrystallographic symmetry procedures. The envelope from this 4 Å map was then used to construct a polyalanine model from which phases to 3.5 Å were calculated.

Three additional virus examples include: (1) The crystallographic analysis of the core of bluetongue virus (BTV), in which the cryo EM map of the BTV core (Prasad *et al.*, 1992) was used to position the X-ray-derived structure of the VP7 capsid protein so that a pseudo-atomic model could be generated (Grimes *et al.*, 1997). This model was then used to calculate initial phases for the X-ray data for the whole core (Grimes *et al.*, 1998). (2) The cryo EM derived map of human rhinovirus type 14 (HRV14) complexed with neutralizing Fab 17-1A (Liu *et al.*, 1994) was used in the solution of the X-ray structure of the same complex. Here, the structures of the isolated Fab and the uncomplexed virus had been solved previously. The EM map of the HRV–Fab complex was used to position these components and provide a pseudo-atomic phasing model for the X-ray data (Smith *et al.*, 1996). (3) The EM structure for the hepatitis B cores at 7.4 Å (Böttcher, Wynne & Crowther, 1997) was used to provide initial phasing for solving the atomic structure by X-ray crystallography at 3.3 Å (Wynne *et al.*, 1999).

Two non-viral examples of the use of EM data in X-ray crystallography include: (1) The structure of bacteriorhodopsin, solved at 3.5 and 3.0 Å resolution by electron microscopy (Grigorieff *et al.*, 1996; Kimura *et al.*, 1997), was used to allow solution of several 3D crystal forms by molecular replacement

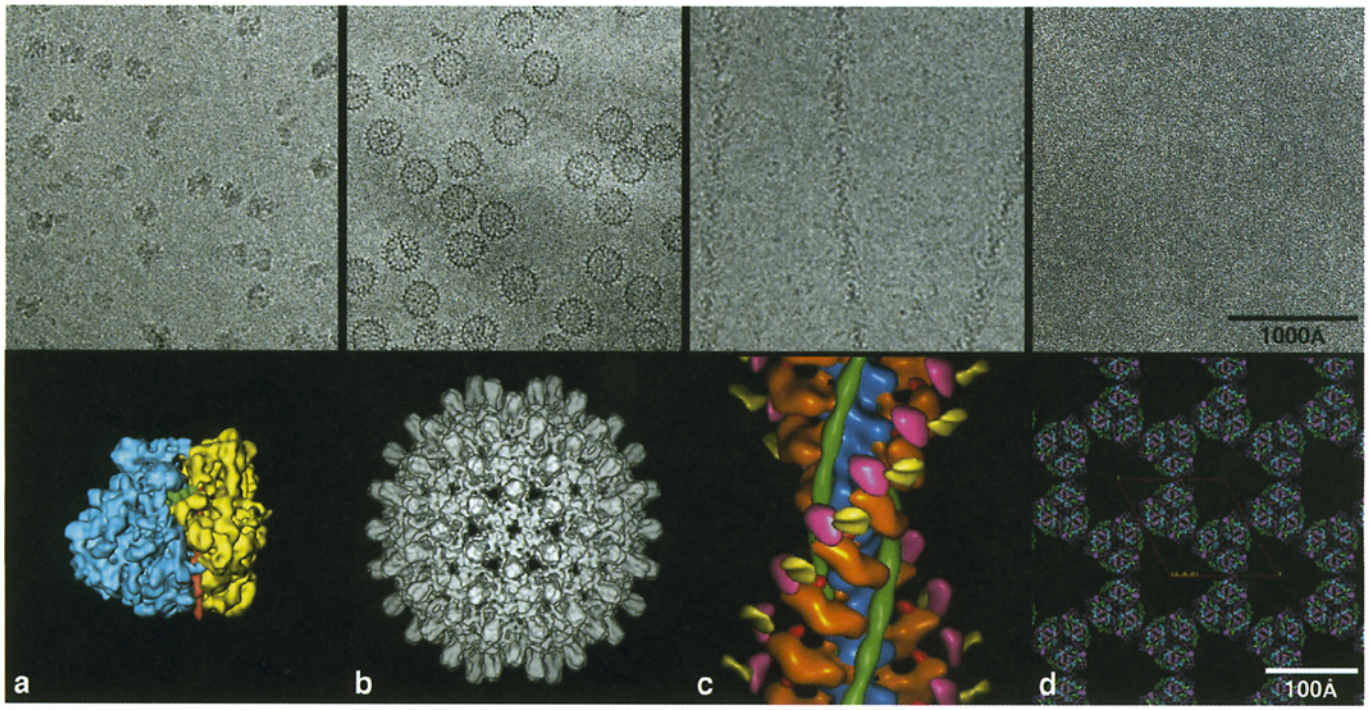

Fig. 19.6.5.1. Examples of macromolecules studied by cryo EM and 3D image reconstruction and the resulting 3D structures (bottom row) after cryo EM analysis. All micrographs (top row) are displayed at ~170000× magnification and all models at ~1200000× magnification. (*a*) A single particle without symmetry. The micrograph shows 70S *E. coli* ribosomes complexed with mRNA and fMet-tRNA. The surface-shaded density map, made by averaging 73 000 ribosome images from 287 micrographs, has a resolution of 11.5 Å. The 50S and 30S subunits and the tRNA are coloured blue, yellow and green, respectively. The identity of many of the protein and RNA components is known and some RNA double helices are clearly recognizable by their major and minor grooves (*e.g.* helix 44 is shown in red). Courtesy of J. Frank (SUNY, Albany), using unpublished data from I. Gabashvili, R. Agrawal, C. Spahn, R. Grassucci, J. Frank & P. Penczek. (*b*) A single particle with symmetry. The micrograph shows hepatitis B virus cores. The 3D reconstruction, at a resolution of 7.4 Å, was computed from 6384 particle images taken from 34 micrographs. From Böttcher, Wynne & Crowther (1997). (*c*) A helical filament. The micrograph shows actin filaments decorated with myosin S1 heads containing the essential light chain. The 3D reconstruction, at a resolution of 30–35 Å, is a composite in which the differently coloured parts are derived from a series of difference maps that were superimposed on F-actin. The components include: F-actin (blue), myosin heavy-chain motor domain (orange), essential light chain (purple), regulatory light chain (white), tropomyosin (green) and myosin motor domain N-terminal beta-barrel (red). Courtesy of A. Lin, M. Whittaker & R. Milligan (Scripps Research Institute, La Jolla). (*d*) A 2D crystal: light-harvesting complex LHCII at 3.4 Å resolution. The model shows the protein backbone and the arrangement of chromophores in a number of trimeric subunits in the crystal lattice. In this example, image contrast is too low to see any hint of the structure without image processing (see also Fig. 19.6.4.2). Courtesy of W. Kühlbrandt (Max-Planck-Institute for Biophysics, Frankfurt).

(Pebay-Peyroula *et al.*, 1997; Essen *et al.*, 1998; Luecke *et al.*, 1998). (2) Density maps of the 50S ribosomal subunits from two species obtained by cryo EM (Frank *et al.*, 1995; Ban *et al.*, 1998) were used to help solve the X-ray crystal structure of the *Haloarcula marismortui* 50S subunit (Ban *et al.*, 1998).

19.6.5. Recent trends

The new generation of intermediate-voltage (~300 kV) FEG microscopes becoming available is now making it much easier to obtain higher-resolution images which, by use of larger defocus values, have good image contrast at both very low and very high resolution. The greater contrast at low resolution greatly facilitates particle-alignment procedures, and the increased contrast resulting from the high-coherence illumination helps to increase the signal-to-noise ratio for the structure at high resolution. Cold stages are constantly being improved, with several liquid-helium stages now in operation (*e.g.* Fujiyoshi *et al.*, 1991; Zemlin *et al.*, 1996). Two of these are commercially available from JEOL and FEI/Philips/Gatan. The microscope vacuums are improving so that the bugbear of ice contamination in the microscope, which prevents prolonged work on the same grid, is likely to disappear soon. The improved drift and vibration performance of the cold stage means longer (and therefore more coherently illuminated) exposures at higher resolution can be recorded more easily. Hopefully, the first atomic structure of a single-particle macromolecular assembly solved by electron microscopy will soon become a reality.

Finally, three additional likely trends include: (1) increased automation, including the recording of micrographs, and the use of spot-scan procedures in remote microscope operation (Kisseberth *et al.*, 1997; Hadida-Hassan *et al.*, 1999) and in every aspect of image processing; (2) production of better electronic cameras (*e.g.* CCD or pixel detectors); and (3) increased use of dose-fractionated, tomographic tilt series to extend EM studies to the domain of larger supramolecular and cellular structures (McEwen *et al.*, 1995; Baumeister *et al.*, 1999).

Acknowledgements

We are greatly indebted to all our colleagues at Purdue and Cambridge for their insightful comments and suggestions, to B. Böttcher, R. Crowther, J. Frank, W. Kühlbrandt and R. Milligan for supplying images used in Fig. 19.6.5.1, which gives some examples of the best work done recently, and J. Brightwell for editorial assistance. TSB was supported in part by grant GM33050 from the National Institutes of Health.

19.5 (*cont.*)

Hendrickson, W. A. (1985). *Stereochemically restrained refinement of macromolecular structures. Methods Enzymol.* **115**, 252–270.

Holmes, K. C., Popp, D., Gebhard, W. & Kabsch, W. (1990). *Atomic model of the actin filament. Nature (London)*, **347**, 44–49.

Inouye, H., Fraser, P. E. & Kirschner, D. A. (1993). *Structure of β-crystallite assemblies formed by Alzheimer β-amyloid protein analogs – analysis by X-ray diffraction. Biophys. J.* **64**, 502–519.

Ivanova, M. I. & Makowski, L. (1998). *Iterative low-pass filtering for estimation of the background in fiber diffraction patterns. Acta Cryst.* A**54**, 626–631.

Klug, A., Crick, F. H. C. & Wyckoff, H. W. (1958). *Diffraction from helical structures. Acta Cryst.* **11**, 199–212.

Lorenz, M. & Holmes, K. C. (1993). *Computer processing and analysis of X-ray fiber diffraction data. J. Appl. Cryst.* **26**, 82–91.

MacGillavry, C. H. & Bruins, E. M. (1948). *On the Patterson transforms of fibre diagrams. Acta Cryst.* **1**, 156–158.

Makowski, L. (1978). *Processing of X-ray diffraction data from partially oriented specimens. J. Appl. Cryst.* **11**, 273–283.

Makowski, L., Caspar, D. L. D. & Marvin, D. A. (1980). *Filamentous bacteriophage Pf1 structure determined at 7 Å resolution by refinement of models for the α-helical subunit. J. Mol. Biol.* **140**, 149–181.

Malinchik, S. B., Inouye, H., Szumowski, K. E. & Kirschner, D. A. (1998). *Structural analysis of Alzheimer's β(1–40) amyloid: protofilament assembly of tubular fibrils. Biophys. J.* **74**, 537–545.

Marvin, D. A., Wiseman, R. L. & Wachtel, E. J. (1974). *Filamentous bacterial viruses. XI. Molecular architecture of the class II (Pf1, Xf) virion. J. Mol. Biol.* **82**, 121–138.

Meyer, K. H. & Misch, L. (1937). *Positions des atomes dans le nouveau modèle spatial de la cellulose. Helv. Chim. Acta*, **20**, 232–244.

Millane, R. P. (1989). *R factors in X-ray fiber diffraction. II. Largest likely R factors. Acta Cryst.* A**45**, 573–576.

Millane, R. P. & Arnott, S. (1985). *Background removal in X-ray fiber diffraction patterns. J. Appl. Cryst.* **18**, 419–423.

Millane, R. P. & Arnott, S. (1986). *Digital processing of X-ray diffraction patterns from oriented fibers. J. Macromol. Sci. Phys.* B**24**, 193–227.

Namba, K., Pattanayak, R. & Stubbs, G. (1989). *Visualization of protein–nucleic acid interactions in a virus: refinement of intact tobacco mosaic virus at 2.9 Å resolution by fiber diffraction data. J. Mol. Biol.* **208**, 307–325.

Namba, K. & Stubbs, G. (1985). *Solving the phase problem in fiber diffraction. Application to tobacco mosaic virus at 3.6 Å resolution. Acta Cryst.* A**41**, 252–262.

Namba, K. & Stubbs, G. (1987*a*). *Isomorphous replacement in fiber diffraction using limited numbers of heavy-atom derivatives. Acta Cryst.* A**43**, 64–69.

Namba, K. & Stubbs, G. (1987*b*). *Difference Fourier syntheses in fiber diffraction. Acta Cryst.* A**43**, 533–539.

Nambudripad, R., Stark, W. & Makowski, L. (1991). *Neutron diffraction studies of the structure of filamentous bacteriophage Pf1 – demonstration that the coat protein consists of a pair of α-helices with an intervening, non-helical loop. J. Mol. Biol.* **220**, 359–379.

Okuyama, K., Obata, Y., Noguchi, K., Kusaba, T., Ito, Y. & Ohno, S. (1996). *Single helical structure of curdlan triacetate. Biopolymers*, **38**, 557–566.

Pauling, L. & Corey, R. B. (1951). *Atomic coordinates and structure factors for two helical configurations of polypeptide chains. Proc. Natl Acad. Sci. USA*, **37**, 235–240.

Pauling, L. & Corey, R. B. (1953). *Two rippled-sheet configurations of polypeptide chains, and a note about the pleated sheets. Proc. Natl Acad. Sci. USA*, **39**, 253–256.

Ramachandran, G. N. & Kartha, G. (1955). *Structure of collagen. Nature (London)*, **176**, 593–595.

Rich, A. & Crick, F. H. C. (1955). *The structure of collagen. Nature (London)*, **176**, 915–916.

Shotton, M. W., Pope, L. H., Forsyth, V. T., Denny, R. C., Archer, J., Langan, P., Ye, H. & Boote, C. (1998). *New developments in instrumentation for X-ray and neutron fibre diffraction experiments. J. Appl. Cryst.* **31**, 758–766.

Smith, P. J. C. & Arnott, S. (1978). *LALS: a linked-atom least-squares reciprocal-space refinement system incorporating stereochemical restraints to supplement sparse diffraction data. Acta Cryst.* A**34**, 3–11.

Squire, J. M., Al-Khayat, H. A. & Yagi, N. (1993). *Muscle thin filament structure and regulation. Actin sub-domain movements and the tropomyosin shift modelled from low-angle X-ray diffraction. J. Chem. Soc. Faraday Trans.* **89**, 2717–2726.

Stroud, W. J. & Millane, R. P. (1995). *Analysis of disorder in biopolymer fibers. Acta Cryst.* A**51**, 790–800.

Stubbs, G. (1987). *The Patterson function in fiber diffraction.* In *Patterson and Pattersons*, edited by J. P. Glusker, E. K. Patterson & M. Rossi, pp. 548–557. New York: Oxford University Press.

Stubbs, G. (1989). *The probability distributions of X-ray intensities in fiber diffraction: largest likely values for fiber diffraction R factors. Acta Cryst.* A**45**, 254–258.

Stubbs, G. J. & Diamond, R. (1975). *The phase problem for cylindrically averaged diffraction patterns. Solution by isomorphous replacement and application to tobacco mosaic virus. Acta Cryst.* A**31**, 709–718.

Stubbs, G. & Makowski, L. (1982). *Coordinated use of isomorphous replacement and layer-line splitting in the phasing of fiber diffraction data. Acta Cryst.* A**38**, 417–425.

Stubbs, G., Namba, K. & Makowski, L. (1986). *Application of restrained least-squares refinement to fiber diffraction from macromolecular assemblies. Biophys. J.* **49**, 58–60.

Torbet, J. (1987). *Using magnetic orientation to study structure and assembly. Trends Biochem. Sci.* **12**, 327–330.

Walkinshaw, M. D. & Arnott, S. (1981). *Conformations and interactions of pectins. I. X-ray diffraction analysis of sodium pectate in neutral and acidified forms. J. Mol. Biol.* **153**, 1055–1073.

Wang, H., Culver, J. N. & Stubbs, G. (1997). *Structure of ribgrass mosaic virus at 2.9 Å resolution: evolution and taxonomy of tobamoviruses. J. Mol. Biol.* **269**, 769–779.

Wang, H. & Stubbs, G. (1993). *Molecular dynamics in refinement against fiber diffraction data. Acta Cryst.* A**49**, 504–513.

Wang, H. & Stubbs, G. (1994). *Structure determination of cucumber green mottle mosaic virus by X-ray fiber diffraction. Significance for the evolution of tobamoviruses. J. Mol. Biol.* **239**, 371–384.

Watson, J. D. & Crick, F. H. C. (1953). *Molecular structure of nucleic acids. Nature (London)*, **171**, 737–738.

Winter, W. T., Smith, P. J. C. & Arnott, S. (1975). *Hyaluronic acid: structure of a fully extended 3-fold helical sodium salt and comparison with the less extended 4-fold helical forms. J. Mol. Biol.* **99**, 219–235.

Yamashita, I., Hasegawa, K., Suzuki, H., Vonderviszt, F., Mimori-Kiyosue, Y. & Namba, K. (1998). *Structure and switching of bacterial flagellar filaments studied by X-ray fiber diffraction. Nature Struct. Biol.* **5**, 125–132.

Yamashita, I., Suzuki, H. & Namba, K. (1998). *Multiple-step method for making exceptionally well-oriented liquid-crystalline sols of macromolecular assemblies. J. Mol. Biol.* **278**, 609–615.

Yamashita, I., Vonderviszt, F., Mimori, Y., Suzuki, H., Oosawa, K. & Namba, K. (1995). *Radial mass analysis of the flagellar filament of Salmonella: implications for the subunit folding. J. Mol. Biol.* **253**, 547–558.

Zugenmaier, P. & Sarko, A. (1980). *The variable virtual bond modeling technique for solving polymer crystal structures. Am. Chem. Soc. Symp. Ser.* **141**, 225–237.

19.6

Adrian, M., Dubochet, J., Lepault, J. & McDowall, A. W. (1984). *Cryo-electron microscopy of viruses. Nature (London)*, **308**, 32–36.

Agar, A. W., Alderson, R. H. & Chescoe, D. (1974). *Principles and practice of electron microscope operation.* In *Practical methods in electron microscopy*, Vol. 2, edited by A. M. Glauert, pp. 1–345. Amsterdam: North-Holland.

19.6 (*cont.*)

Agard, D. A. (1983). *A least-squares method for determining structure factors in three-dimensional tilted-view reconstructions. J. Mol. Biol.* **167**, 849–852.

Agrawal, R. K., Penczek, P., Grassucci, R. A., Li, Y., Leith, A., Nierhaus, K. H. & Frank, J. (1996). *Direct visualization of A-, P-, and E-site transfer RNAs in the Escherichia coli ribosome. Science*, **271**, 1000–1002.

Amos, L. A., Henderson, R. & Unwin, P. N. T. (1982). *Three-dimensional structure determination by electron microscopy of two-dimensional crystals. Prog. Biophys. Mol. Biol.* **39**, 183–231.

Baker, T. S. & Amos, L. A. (1978). *Structure of the tubulin dimer in zinc-induced sheets. J. Mol. Biol.* **123**, 89–106.

Baker, T. S. & Cheng, R. H. (1996). *A model-based approach for determining orientations of biological macromolecules imaged by cryoelectron microscopy. J. Struct. Biol.* **116**, 120–130.

Baker, T. S. & Johnson, J. E. (1996). *Low resolution meets high: towards a resolution continuum from cells to atoms. Curr. Opin. Struct. Biol.* **6**, 585–594.

Baker, T. S., Newcomb, W. W., Booy, F. P., Brown, J. C. & Steven, A. C. (1990). *Three-dimensional structures of maturable and abortive capsids of equine herpesvirus 1 from cryoelectron microscopy. J. Virol.* **64**, 563–573.

Baker, T. S., Newcomb, W. W., Olson, N. H., Cowsert, L. M., Olson, C. & Brown, J. C. (1991). *Structures of bovine and human papilloma viruses: analysis by cryoelectron microscopy and three-dimensional image reconstruction. Biophys. J.* **60**, 1445–1456.

Baker, T. S., Olson, N. H. & Fuller, S. D. (1999). *Adding the third dimension to virus life cycles: three-dimensional reconstruction of icosahedral viruses from cryo-electron micrographs. Microbiol. Mol. Biol. Rev.* **63**, 862–922.

Baldwin, J. M., Henderson, R., Beckman, E. & Zemlin, F. (1988). *Images of purple membrane at 2.8 Å resolution obtained by cryo-electron microscopy. J. Mol. Biol.* **202**, 585–591.

Ban, N., Freeborn, B., Nissen, P., Penczek, P., Grassucci, R. A., Sweet, R., Frank, J., Moore, P. B. & Steitz, T. A. (1998). *A 9 Å resolution X-ray crystallographic map of the large ribosomal subunit. Cell*, **93**, 1105–1115.

Baumeister, W., Grimm, R. & Walz, J. (1999). *Electron tomography of molecules and cells. Trends Cell Biol.* **9**, 81–85.

Bellare, J. R., Davis, H. T., Scriven, L. E. & Talmon, Y. (1988). *Controlled environment vitrification system: an improved sample preparation technique. J. Electron Microsc. Tech.* **10**, 87–111.

Belnap, D. M., Olson, N. H. & Baker, T. S. (1997). *A method for establishing the handedness of biological macromolecules. J. Struct. Biol.* **120**, 44–51.

Belnap, D. M., Olson, N. H., Cladel, N. M., Newcomb, W. W., Brown, J. C., Kreider, J. W., Christensen, N. D. & Baker, T. S. (1996). *Conserved features in papillomavirus and polyomavirus capsids. J. Mol. Biol.* **259**, 249–263.

Beroukhim, R. & Unwin, N. (1997). *Distortion correction of tubular crystals: improvements in the acetylcholine receptor structure. Ultramicroscopy*, **70**, 57–81.

Berriman, J. & Unwin, N. (1994). *Analysis of transient structures by cryo-microscopy combined with rapid mixing of spray droplets. Ultramicroscopy*, **56**, 241–252.

Beuron, F., Maurizi, M. R., Belnap, D. M., Kocsis, E., Booy, F. P., Kessel, M. & Steven, A. C. (1998). *At sixes and sevens: characterization and the symmetry mismatch of the ClpAP chaperone-assisted protease. J. Struct. Biol.* **123**, 248–259.

Bloomer, A. C., Graham, J., Hovmoller, S., Butler, P. J. G. & Klug, A. (1978). *Protein disk of tobacco mosaic virus at 2.8 Å resolution showing the interactions within and between subunits. Nature (London)*, **276**, 362–368.

Boier Martin, I. M., Marinescu, D. C., Lynch, R. E. & Baker, T. S. (1997). *Identification of spherical virus particles in digitized images of entire electron micrographs. J. Struct. Biol.* **120**, 146–157.

Böttcher, B., Kiselev, N. A., Stel'mashchuk, V. Y., Perevozchikova, N. A., Borisov, A. V. & Crowther, R. A. (1997). *Three-dimensional structure of infectious bursal disease virus determined by electron cryomicroscopy. J. Virol.* **71**, 325–330.

Böttcher, B., Tsuji, N., Takahashi, H., Dyson, M. R., Zhao, S., Crowther, R. A. & Murray, K. (1998). *Peptides that block hepatitis B virus assembly: analysis by cryomicroscopy, mutagenesis and transfection. EMBO J.* **17**, 6839–6845.

Böttcher, B., Wynne, S. A. & Crowther, R. A. (1997). *Determination of the fold of the core protein of hepatitis B virus by electron microscopy. Nature (London)*, **386**, 88–91.

Brenner, S. & Horne, R. W. (1959). *A negative staining method for high resolution electron microscopy of viruses. Biochem. Biophys. Acta Protein Struct.* **34**, 103–110.

Brink, J., Sherman, M. B., Berriman, J. & Chiu, W. (1998). *Evaluation of charging on macromolecules in electron cryomicroscopy. Ultramicroscopy*, **72**, 41–52.

Brünger, A. T., Kuriyan, J. & Karplus, M. (1987). *Crystallographic R factor refinement by molecular dynamics. Science*, **235**, 458–460.

Carragher, B., Whittaker, M. & Milligan, R. A. (1996). *Helical processing using PHOELIX. J. Struct. Biol.* **116**, 107–112.

Carrascosa, J. L. & Steven, A. C. (1978). *A procedure for evaluation of significant structural differences between related arrays of protein molecules. Micron*, **9**, 199–206.

Castón, J. R., Belnap, D. M., Steven, A. C. & Trus, B. L. (1999). *A strategy for determining the orientations of refractory particles for reconstruction from cryo-electron micrographs with particular reference to round, smooth-surfaced, icosahedral viruses. J. Struct. Biol.* **125**, 209–215.

Che, Z., Olson, N. H., Leippe, D., Lee, W.-M., Mosser, A. G., Rueckert, R. R., Baker, T. S. & Smith, T. J. (1998). *Antibody-mediated neutralization of human rhinovirus 14 explored by means of cryoelectron microscopy and X-ray crystallography of virus–Fab complexes. J. Virol.* **72**, 4610–4622.

Cheng, A., van Hoek, A. N., Yeager, M., Verkman, A. S. & Mitra, A. K. (1997). *Three-dimensional organization of a human water channel. Nature (London)*, **387**, 627–630.

Cheng, R. H., Kuhn, R. J., Olson, N. H., Rossmann, M. G., Choi, H.-K., Smith, T. J. & Baker, T. S. (1995). *Nucleocapsid and glycoprotein organization in an enveloped virus. Cell*, **80**, 621–630.

Cheng, R. H., Olson, N. H. & Baker, T. S. (1992). *Cauliflower mosaic virus, a 420 subunit ($T = 7$), multi-layer structure. Virology*, **186**, 655–668.

Cheng, R. H., Reddy, V. S., Olson, N. H., Fisher, A. J., Baker, T. S. & Johnson, J. E. (1994). *Functional implications of quasi-equivalence in a $T = 3$ icosahedral animal virus established by cryo-electron microscopy and X-ray crystallography. Structure*, **2**, 271–282.

Chiu, W. (1986). *Electron microscopy of frozen, hydrated biological specimens. Annu. Rev. Biophys. Biophys. Chem.* **15**, 237–257.

Conway, J. F., Cheng, N., Zlotnick, A., Stahl, S. J., Wingfield, P. T., Belnap, D. M., Kanngiesser, U., Noah, M. & Steven, A. C. (1998). *Hepatitis B virus capsid: localization of the putative immunodominant loop (residues 78 to 83) on the capsid surface, and implications for the distinction between c and e-antigens. J. Mol. Biol.* **279**, 1111–1121.

Conway, J. F. & Steven, A. C. (1999). *Methods for reconstructing density maps of 'single' particles from cryoelectron micrographs to subnanometer resolution. J. Struct. Biol.* **128**, 106–118.

Conway, J. F., Trus, B. L., Booy, F. P., Newcomb, W. W., Brown, J. C. & Steven, A. C. (1996). *Visualization of three-dimensional density maps reconstructed from cryoelectron micrographs of viral capsids. J. Struct. Biol.* **116**, 200–208.

Cowley, J. M. (1975). *Diffraction physics*. Amsterdam: North-Holland.

Crowther, R. A. (1971). *Procedures for three-dimensional reconstruction of spherical viruses by Fourier synthesis from electron micrographs. Philos. Trans. R. Soc. London*, **261**, 221–230.

Crowther, R. A., Amos, L. A., Finch, J. T., DeRosier, D. J. & Klug, A. (1970). *Three dimensional reconstructions of spherical viruses by Fourier synthesis from electron micrographs. Nature (London)*, **226**, 421–425.

19.6 (*cont.*)

Crowther, R. A., Henderson, R. & Smith, J. M. (1996). *MRC image processing programs. J. Struct. Biol.* **116**, 9–16.

Crowther, R. A., Kiselev, N. A., Böttcher, B., Berriman, J. A., Borisova, G. P., Ose, V. & Pumpens, P. (1994). *Three-dimensional structure of hepatitis B virus core particles determined by electron cryomicroscopy. Cell*, **77**, 943–950.

Crowther, R. A. & Luther, P. K. (1984). *Three-dimensional reconstruction from a single oblique section of fish muscle M-band. Nature (London)*, **307**, 569–570.

Cyrklaff, M. & Kühlbrandt, W. (1994). *High resolution electron microscopy of biological specimens in cubic ice. Ultramicroscopy*, **55**, 141–153.

DeRosier, D. J. & Klug, A. (1968). *Reconstruction of three dimensional structures from electron micrographs. Nature (London)*, **217**, 130–134.

DeRosier, D. J. & Moore, P. B. (1970). *Reconstruction of three-dimensional images from electron micrographs of structures with helical symmetry. J. Mol. Biol.* **52**, 355–369.

Downing, K. H. (1991). *Spot-scan imaging in transmission electron microscopy. Science*, **251**, 53–59.

Dryden, K. A., Wang, G., Yeager, M., Nibert, M. L., Coombs, K. M., Furlong, D. B., Fields, B. N. & Baker, T. S. (1993). *Early steps in reovirus infection are associated with dramatic changes in supramolecular structure and protein conformation: analysis of virions and subviral particles by cryoelectron microscopy and image reconstruction. J. Cell Biol.* **122**, 1023–1041.

Dubochet, J., Adrian, M., Chang, J.-J., Homo, J.-C., Lepault, J., McDowall, A. W. & Schultz, P. (1988). *Cryo-electron microscopy of vitrified specimens. Q. Rev. Biophys.* **21**, 129–228.

Dubochet, J., Chang, J.-J., Freeman, R., Lepault, J. & McDowall, A. W. (1982). *Frozen aqueous suspensions. Ultramicroscopy*, **10**, 55–62.

Dubochet, J., Groom, M. & Müller-Neuteboom, S. (1982). *The mounting of macromolecules for electron microscopy with particular reference to surface phenomena and the treatment of support films by glow discharge. Adv. Opt. Electron Microsc.* **8**, 107–135.

Dubochet, J., Lepault, J., Freeman, R., Berriman, J. A. & Homo, J.-C. (1982). *Electron microscopy of frozen water and aqueous solutions. J. Microsc.* **128**, 219–237.

Egelman, E. H. (1986). *An algorithm for straightening images of curved filamentous structures. Ultramicroscopy*, **19**, 367–374.

Erickson, H. P. & Klug, A. (1971). *Measurement and compensation of defocusing and aberrations by Fourier processing of micrographs. Philos. Trans. R. Soc. London Ser. B*, **261**, 105–118.

Essen, L. O., Siegert, R., Lehmann, W. D. & Oesterhelt, D. (1998). *Lipid patches in membrane protein oligomers: crystal structure of the bacteriorhodopsin–lipid complex. Proc. Natl Acad. Sci. USA*, **95**, 11673–11678.

Finch, J. T. (1972). *The hand of the helix of tobacco mosaic virus. J. Mol. Biol.* **66**, 291–294.

Frank, J. (1973). *The envelope of electron microscopic transfer functions for partially coherent illumination. Optik*, **38**, 519–536.

Frank, J. (1992). Editor. *Electron tomography: three-dimensional imaging with the transmission electron microscope*. New York: Plenum Press.

Frank, J. (1996). *Three-dimensional electron microscopy of macromolecular assemblies*. San Diego: Academic Press.

Frank, J. (1997). *The ribosome at higher resolution – the donut takes shape. Curr. Opin. Struct. Biol.* **7**, 266–272.

Frank, J., Heagle, A. B. & Agrawal, R. K. (1999). *Animation of the dynamical events of the elongation cycle based on cryoelectron microscopy of functional complexes of the ribosome. J. Struct. Biol.* **128**, 15–18.

Frank, J., Radermacher, M., Penczek, P., Zhu, J., Li, Y., Ladjadj, M. & Leith, A. (1996). *SPIDER and WEB: processing and visualization of images in 3D electron microscopy and related fields. J. Struct. Biol.* **116**, 190–199.

Frank, J., Verschoor, A. & Boublik, M. (1981). *Computer averaging of electron micrographs of 40S ribosomal subunits. Science*, **214**, 1353–1355.

Frank, J., Zhu, J., Penczek, P., Li, Y., Srivastava, S., Verschoor, A., Radermacher, M., Grassucci, R., Lata, R. K. & Agrawal, R. K. (1995). *A model of protein synthesis based on cryo-electron microscopy of the E. coli ribosome. Nature (London)*, **376**, 441–444.

Fujiyoshi, Y., Mizusaki, T., Morikawa, K., Yamagishi, H., Aoki, Y., Kihara, H. & Harada, Y. (1991). *Development of a superfluid helium stage for high-resolution electron microscopy. Ultramicroscopy*, **38**, 241–251.

Fuller, S. D., Berriman, J. A., Butcher, S. J. & Gowen, B. E. (1995). *Low pH induces swiveling of the glycoprotein heterodimers in the Semiliki forest virus spike complex. Cell*, **81**, 715–725.

Fuller, S. D., Butcher, S. J., Cheng, R. H. & Baker, T. S. (1996). *Three-dimensional reconstruction of icosahedral particles – the uncommon line. J. Struct. Biol.* **116**, 48–55.

Fung, J. C., Liu, W., DeRuijter, W. J., Chen, H., Abbey, C. K., Sedat, J. W. & Agard, D. A. (1996). *Toward fully automated high-resolution electron tomography. J. Struct. Biol.* **116**, 181–189.

Gabashvili, I. S., Agrawal, R. K., Spahn, C. M. T., Grassucci, R. A., Svergun, D. I., Frank, J. & Penczek, P. (2000). *Solution structure of the E. coli 70S ribosome at 11.5 Å resolution. Cell*, **100**, 537–549.

Glaeser, R. M. (1971). *Limitations to significant information in biological electron microscopy as a result of radiation damage. J. Ultrastruct. Res.* **36**, 466–482.

Glaeser, R. M. (1985). *Electron crystallography of biological macromolecules. Annu. Rev. Phys. Chem.* **36**, 243–275.

Grant, R. A., Filman, D. J., Finkel, S. E., Kolter, R. & Hogle, J. M. (1998). *The crystal structure of Dps, a ferritin homolog that binds and protects DNA. Nature Struct. Biol.* **5**, 294–303.

Grigorieff, N. (1998). *Three-dimensional structure of bovine NADH:ubiquinone oxidoreductase (complex I) at 22 Å in ice. J. Mol. Biol.* **277**, 1033–1046.

Grigorieff, N., Ceska, T. A., Downing, K. H., Baldwin, J. M. & Henderson, R. (1996). *Electron-crystallographic refinement of the structure of bacteriorhodopsin. J. Mol. Biol.* **259**, 393–421.

Grimes, J. M., Burroughs, J. N., Gouet, P., Diprose, J. M., Malby, R., Ziéntara, S., Mertens, P. P. C. & Stuart, D. I. (1998). *The atomic structure of the bluetongue virus core. Nature (London)*, **395**, 470–478.

Grimes, J. M., Jakana, J., Ghosh, M., Basak, A. K., Roy, P., Chiu, W., Stuart, D. I. & Prasad, B. V. V. (1997). *An atomic model of the outer layer of the bluetongue virus core derived from X-ray crystallography and electron cryomicroscopy. Structure*, **5**, 885–893.

Haas, F. de, Kuchomov, A., Traveau, J.-C., Boisset, N., Vinogradov, S. N. & Lamy, J. N. (1997). *Three-dimensional reconstruction of native and reassembled Lumbricus terrestris extracellular hemoglobin. Location of the monomeric globin chains. Biochemistry*, **36**, 7330–7338.

Hadida-Hassan, M., Young, S. J., Peltier, S. T., Wong, M., Lamont, S. & Ellisman, M. H. (1999). *Web-based telemicroscopy. J. Struct. Biol.* **125**, 235–245.

Hardt, S., Wang, B. & Schmid, M. F. (1996). *A brief description of I.C.E.: the integrated crystallographic environment. J. Struct. Biol.* **116**, 68–70.

Hargittai, I. & Hargittai, M. (1988). Editors. *Stereochemical applications of gas-phase electron diffraction*. New York: VCH.

Hasler, L., Heymann, J. B., Engel, A., Kistler, J. & Walz, T. (1998). *2D crystallization of membrane proteins: rationales and examples. J. Struct. Biol.* **121**, 162–171.

Havelka, W. A., Henderson, R. & Oesterhelt, D. (1995). *Three-dimensional structure of halorhodopsin at 7 Å resolution. J. Mol. Biol.* **247**, 726–738.

Heel, M. van (1987*a*). *Angular reconstitution: a posteriori assignment of projection directions for 3D reconstruction. Ultramicroscopy*, **21**, 111–124.

Heel, M. van (1987*b*). *Similarity measures between images. Ultramicroscopy*, **21**, 95–100.

19.6 (*cont.*)

Heel, M. van & Frank, J. (1981). *Use of multivariate statistics in analyzing the images of biological macromolecules. Ultramicroscopy*, **6**, 187–194.

Heel, M. van, Harauz, G. & Orlova, E. V. (1996). *A new generation of the IMAGIC image processing system. J. Struct. Biol.* **116**, 17–24.

Heel, M. van & Hollenberg, J.(1980). *On the stretching of distorted images of two-dimensional crystals.* In *Electron microscopy at molecular dimensions*, edited by W. Baumeister & W. Vogell, pp. 256–260. Berlin: Springer-Verlag.

Henderson, R. (1995). *The potential and limitations of neutrons, electrons, and X-rays for atomic resolution microscopy of unstained biological molecules. Q. Rev. Biophys.* **28**, 171–193.

Henderson, R., Baldwin, J. M., Ceska, T. A., Zemlin, F., Beckmann, E. & Downing, K. H. (1990). *Model for the structure of bacteriorhodopsin based on high-resolution electron cryo-microscopy. J. Mol. Biol.* **213**, 899–929.

Henderson, R., Baldwin, J. M., Downing, K. H., Lepault, J. & Zemlin, F. (1986). *Structure of purple membrane from halobacterium: recording, measurement, and evaluation of electron micrographs at 3.5 Å resolution. Ultramicroscopy*, **19**, 147–178.

Henderson, R. & Unwin, P. N. T. (1975). *Three-dimensional model of purple membrane obtained by electron microscopy. Nature (London)*, **257**, 28–32.

Hewat, E. A., Verdaguer, N., Fita, I., Blakemore, W., Brookes, S., King, A., Newman, J., Domingo, E., Mateu, M. G. & Stuart, D. I. (1997). *Structure of the complex of an Fab fragment of a neutralizing antibody with foot-and-mouth disease virus: positioning of a highly mobile antigenic group. EMBO J.* **16**, 1492–1500.

Hirose, K., Amos, W. B., Lockhart, A., Cross, R. A. & Amos, L. A. (1997). *Three-dimensional cryoelectron microscopy of 16-protofilament microtubules: structure, polarity, and interaction with motor proteins. J. Struct. Biol.* **118**, 140–148.

Hoenger, A. & Milligan, R. A. (1997). *Motor domains of kinesin and ncd interact with microtubule protofilaments with the same binding geometry. J. Mol. Biol.* **265**, 553–564.

Homo, J.-C., Booy, F., Labouesse, P., Lepault, J. & Dubochet, J. (1984). *Improved anticontaminator for cryo-electron microscopy with a Philips EM 400. J. Microsc.* **136**, 337–340.

Hoppe, W., Langer, R., Knesch, G. & Poppe, C. (1968). *Proteinkristallstrukturanalyse mit elektronenstrahlen. Naturwissenschaften*, **55**, 333–336.

Horne, R. W. & Pasquali-Ronchetti, I. (1974). *A negative staining-carbon film technique for studying viruses in the electron microscope. J. Ultrastruct. Res.* **47**, 361–383.

Huxley, H. E. & Zubay, G. (1960). *Electron microscope observations on the structure of microsomal particles from Escherichia coli. J. Mol. Biol.* **2**, 10–18.

Ilag, L. L., Olson, N. H., Dokland, T., Music, C. L., Cheng, R. H., Bowen, Z., McKenna, R., Rossmann, M. G., Baker, T. S. & Incardona, N. L. (1995). *DNA packaging intermediates of bacteriophage φ X174. Structure*, **3**, 353–363.

Isaacson, M., Langmore, J. & Rose, H. (1974). *Determination of the non-localization of the inelastic scattering of electrons by electron microscopy. Optik*, **41**, 92–96.

Jacobson, R. H., Zhang, X.-J., DuBose, R. F. & Matthews, B. W. (1994). *Three-dimensional structure of β-galactosidase from E. coli. Nature (London)*, **369**, 761–766.

Jap, B., Zulauf, M., Scheybani, T., Hefti, A., Baumeister, W. & Aebi, U. (1992). *2D crystallization: from art to science. Ultramicroscopy*, **46**, 45–84.

Jeng, T.-W., Crowther, R. A., Stubbs, G. & Chui, W. (1989). *Visualization of alpha-helices in tobacco mosaic virus by cryo-electron microscopy. J. Mol. Biol.* **205**, 251–257.

Jones, T. A., Zou, J.-Y., Cowan, S. W. & Kjeldgaard, M. (1991). *Improved methods for building protein models in electron density maps and the location of errors in these models. Acta Cryst.* A**47**, 110–119.

Kenney, J., Karsenti, E., Gowen, B. & Fuller, S. D. (1997). *Three-dimensional reconstruction of the mammalian centriole from cryoelectron micrographs: the use of common lines for orientation and alignment. J. Struct. Biol.* **120**, 320–328.

Kimura, Y., Vassylyev, D. G., Miyazawa, A., Kidera, A., Matsushima, M., Mitsuoka, K., Murata, K., Hirai, T. & Fujiyoshi, Y. (1997). *Surface of bacteriorhodopsin revealed by high-resolution electron crystallography. Nature (London)*, **389**, 206–211.

Kisseberth, N., Whittaker, M., Weber, D., Potter, C. S. & Carragher, B. (1997). *emScope: a tool kit for control and automation of a remote electron microscope. J. Struct. Biol.* **120**, 309–319.

Klug, A. & Berger, J. E. (1964). *An optical method for the analysis of periodicities in electron micrographs, and some observations on the mechanism of negative staining. J. Mol. Biol.* **10**, 565–569.

Kolodziej, S. J., Klueppelberg, H. U., Nolasco, N., Ehses, W., Strickland, D. K. & Stoops, J. K. (1998). *Three-dimensional structure of the human plasmin α_2-macroglobulin complex. J. Struct. Biol.* **123**, 124–133.

Kong, L. B., Siva, A. C., Rome, L. H. & Stewart, P. L. (1999). *Structure of the vault, a ubiquitous cellular component. Structure*, **7**, 371–379.

Kornberg, R. & Darst, S. A. (1991). *Two dimensional crystals of proteins on liquid layers. Curr. Opin. Struct. Biol.* **1**, 642–646.

Koster, A. J., Grimm, R., Typke, D., Hegerl, R., Stoschek, A., Walz, J. & Baumeister, W. (1997). *Perspectives of molecular and cellular electron tomography. J. Struct. Biol.* **120**, 276–308.

Krivanek, O. L. & Mooney, P. E. (1993). *Applications of slow-scan CCD cameras in transmission electron microscopy. Ultramicroscopy*, **49**, 95–108.

Kubalek, E. W., LeGrice, S. F. J. & Brown, P. O. (1994). *Two-dimensional crystallization of histidine-tagged, HIV-1 reverse transcriptase promoted by a novel nickel-chelating lipid. J. Struct. Biol.* **113**, 117–123.

Kühlbrandt, W., Wang, D. N. & Fujiyoshi, Y. (1994). *Atomic model of plant light-harvesting complex by electron crystallography. Nature (London)*, **367**, 614–621.

Langmore, J. P. & Smith, M. F. (1992). *Quantitative energy-filtered electron microscopy of biological molecules in ice. Ultramicroscopy*, **46**, 349–373.

Lawton, J. A., Estes, M. K. & Prasad, B. V. V. (1997). *Three-dimensional visualization of mRNA release from actively transcribing rotavirus particles. Nature Struct. Biol.* **4**, 118–121.

Lawton, J. A. & Prasad, B. V. V. (1996). *Automated software package for icosahedral virus reconstruction. J. Struct. Biol.* **116**, 209–215.

Lepault, J., Booy, F. P. & Dubochet, J. (1983). *Electron microscopy of frozen biological specimens. J. Microsc.* **129**, 89–102.

Liu, H., Smith, T. J., Lee, W.-M., Mosser, A. G., Rueckert, R. R., Olson, N. H., Cheng, R. H. & Baker, T. S. (1994). *Structure determination of an Fab fragment that neutralizes human rhinovirus 14 and analysis of the Fab–virus complex. J. Mol. Biol.* **240**, 127–137.

Luecke, H., Richter, H. T. & Lanyi, J. K. (1998). *Proton transfer pathways in bacteriorhodopsin at 2.3 Å resolution. Science*, **280**, 1934–1937.

Luo, C., Butcher, S. & Bamford, D. H. (1993). *Isolation of a phospholipid-free protein shell of bacteriophage PRD1, an Escherichia coli virus with an internal membrane. Virology*, **194**, 564–569.

McEwen, B. F., Downing, K. H. & Glaeser, R. M. (1995). *The relevance of dose-fractionation in tomography of radiation-sensitive specimens. Ultramicroscopy*, **60**, 357–373.

Mancini, E. J., de Haas, F. & Fuller, S. D. (1997). *High-resolution icosahedral reconstruction: fulfilling the promise of cryo-electron microscopy. Structure*, **5**, 741–750.

Mattevi, A., Obmolova, G., Schulze, E., Kalk, K. H., Westphal, A. H., de Kok, A. & Hol, W. G. J. (1992). *Atomic structure of the cubic core of the pyruvate dehydrogenase multienzyme complex. Science*, **255**, 1544–1550.

Mayer, E. & Astl, G. (1992). *Limits of cryofixation as seen by Fourier transform infrared spectra of metmyoglobin azide and carbonyl hemoglobin in vitrified and freeze concentrated aqueous solution. Ultramicroscopy*, **45**, 185–197.

19.6 (*cont.*)

Metoz, F., Arnal, I. & Wade, R. H. (1997). *Tomography without tilt: three-dimensional imaging of microtubule/motor complexes. J. Struct. Biol.* **118**, 159–168.

Milligan, R. A. (1996). *Protein–protein interactions in the rigor actomyosin complex. Proc. Natl Acad. Sci. USA*, **93**, 21–26.

Miyazawa, A., Fujiyoshi, Y., Stowell, M. & Unwin, N. (1999). *Nicotinic acetylcholine receptor at 4.6 Å resolution: transverse tunnels in the channel wall. J. Mol. Biol.* **288**, 765–786.

Morgan, D. G. & DeRosier, D. (1992). *Processing images of helical structures: a new twist. Ultramicroscopy*, **46**, 263–285.

Namba, K. & Vonderviszt, F. (1997). *Molecular architecture of bacterial flagellum. Q. Rev. Biophys.* **30**, 1–65.

Nogales, E., Wolf, S. G. & Downing, K. H. (1997). *Visualizing the secondary structure of tubulin: three-dimensional map at 4 Å. J. Struct. Biol.* **118**, 119–127.

Nogales, E., Wolf, S. G. & Downing, K. H. (1998). *Structure of the $\alpha\beta$ tubulin dimer by electron crystallography. Nature (London)*, **391**, 199–203.

Olins, D. E., Olins, A. L., Levy, H. A., Durfee, R. C., Margle, S. M., Tinnel, E. P. & Dover, S. D. (1983). *Electron microscopy tomography: transcription in three dimensions. Science*, **220**, 498–500.

Olson, N. H. & Baker, T. S. (1989). *Magnification calibration and the determination of spherical virus diameters using cryo-microscopy. Ultramicroscopy*, **30**, 281–298.

Olson, N. H., Chipman, P. R., Bloom, M. E., McKenna, R., Agbandje-McKenna, M., Booth, T. F. & Baker, T. S. (1997). *Automated CCD data collection and 3D reconstruction of Aleutian mink disease parvovirus.* In *Microscopy and microanalysis*, Vol. 3, Supplement 2, *Proceedings: Microscopy & microanalysis '97*, Cleveland, Ohio, 10–14 August, 1997, pp. 1117–1118. Cleveland, Ohio: Microscopy Society of America/ Springer.

Owen, C. H., Morgan, D. G. & DeRosier, D. J. (1996). *Image analysis of helical objects: the Brandeis helical package. J. Struct. Biol.* **116**, 167–175.

Pebay-Peyroula, E., Rummel, G., Rosenbusch, J. P. & Landau, E. M. (1997). *X-ray structure of bacteriorhodopsin at 2.5 angstroms from microcrystals grown in lipidic cubic phases. Science*, **277**, 1676–1681.

Penczek, P., Radermacher, M. & Frank, J. (1992). *Three-dimensional reconstruction of single particles embedded in ice. Ultramicroscopy*, **40**, 33–53.

Penczek, P. A., Grassucci, R. A. & Frank, J. (1994). *The ribosome at improved resolution: new techniques for merging and orientation refinement in 3D cryo-electron microscopy of biological particles. Ultramicroscopy*, **53**, 251–270.

Polyakov, A., Richter, C., Malhotra, A., Koulich, D., Borukhov, S. & Darst, S. A. (1998). *Visualization of the binding site for the transcript cleavage factor GreB on Escherichia coli RNA polymerase. J. Mol. Biol.* **281**, 465–473.

Prasad, B. V., Yamaguchi, S. & Roy, S. (1992). *Three-dimensional structure of single-shelled bluetongue virus. J. Virol.* **66**, 2135–2142.

Radermacher, M. (1988). *Three-dimensional reconstruction of single particles from random and nonrandom tilt series. J. Electron Microsc. Tech.* **9**, 359–394.

Radermacher, M. (1991). *Three-dimensional reconstruction of single particles in electron microscopy.* In *Image analysis in biology*, edited by D.-P. Hader, pp. 219–246. Boca Raton: CRC Press.

Radermacher, M. (1992). *Weighted back-projection methods.* In *Electron tomography*, edited by J. Frank, pp. 91–115. New York: Plenum Press.

Radermacher, M. (1994). *Three-dimensional reconstruction from random projections: orientational alignment via Radon transforms. Ultramicroscopy*, **53**, 121–136.

Radermacher, M., Wagenknecht, T., Verschoor, A. & Frank, J. (1987). *Three-dimensional reconstructions from a single-exposure, random conical tilt series applied to the 50S ribosomal subunit of Escherichia coli. J. Microsc.* **146**, 113–136.

Reimer, L. (1989). *Transmission electron microscopy.* Berlin: Springer-Verlag.

Reviakine, I., Bergsma-Schutter, W. & Brisson, A. (1998). *Growth of protein 2-D crystals on supported planar lipid bilayers imaged in situ by AFM. J. Struct. Biol.* **121**, 356–361.

Rigaud, J.-L., Mosser, G., Lacapere, J.-J., Olofsson, A., Levy, D. & Ranck, J.-L. (1997). *Bio-beads: an efficient strategy for two-dimensional crystallization of membrane proteins. J. Struct. Biol.* **118**, 226–235.

Schatz, M. & van Heel, M. (1990). *Invariant classification of molecular views in electron micrographs. Ultramicroscopy*, **32**, 255–264.

Schatz, M., Orlova, E. V., Dube, P., Jager, J. & van Heel, M. (1995). *Structure of Lumbricus terrestris hemoglobin at 30 Å resolution determined using angular reconstitution. J. Struct. Biol.* **114**, 28–40.

Shah, A. K. & Stewart, P. L. (1998). *QVIEW: software for rapid selection of particles from digital electron micrographs. J. Struct. Biol.* **123**, 17–21.

Sharma, M. R., Penczek, P., Grassucci, R., Xin, H.-B., Fleisher, S. & Wagenknecht, T. (1998). *Cryoelectron microscopy and image analysis of the cardiac ryanodine receptor. J. Biol. Chem.* **273**, 18429–18434.

Sheehan, B., Fuller, S. D., Pique, M. E. & Yeager, M. (1996). *AVS software for visualization in molecular microscopy. J. Struct. Biol.* **116**, 99–105.

Sherman, M. B., Brink, J. & Chiu, W. (1996). *Performance of a slow-scan CCD camera for macromolecular imaging in a 400 kV electron cryomicroscope. Micron*, **27**, 129–139.

Siegel, D. P. & Epand, R. M. (1997). *The mechanism of lamellar-to-inverted hexagonal phase transitions in phosphatidylethanolamine: implications for membrane fusion mechanisms. Biophys. J.* **73**, 3089–3111.

Siegel, D. P., Green, W. J. & Talmon, Y. (1994). *The mechanism of lamellar-to-inverted hexagonal phase transitions: a study using temperature-jump cryo-electron microscopy. Biophys. J.* **66**, 402–414.

Skoglund, U. & Daneholt, B. (1986). *Electron microscope tomography. Trends Biochem. Sci.* **11**, 499–503.

Skoglund, U., Öfverstedt, L.-G., Burnett, R. M. & Bricogne, G. (1996). *Maximum-entropy three-dimensional reconstruction with deconvolution of the contrast transfer function: a test application with adenovirus. J. Struct. Biol.* **117**, 173–188.

Smith, T. J., Chase, E. S., Schmidt, T. J., Olson, N. H. & Baker, T. S. (1996). *Neutralizing antibody to human rhinovirus 14 penetrates the receptor-binding canyon. Nature (London)*, **383**, 350–354.

Speir, J. A., Munshi, S., Wang, G., Baker, T. S. & Johnson, J. E. (1995). *Structures of the native and swollen forms of cowpea chlorotic mottle virus determined by X-ray crystallography and cryo-electron microscopy. Structure*, **3**, 63–78.

Spence, J. C. H. (1988). *Experimental high-resolution electron microscopy.* Oxford University Press.

Spencer, S. M., Sgro, J.-Y., Dryden, K. A., Baker, T. S. & Nibert, M. L. (1997). *IRIS explorer software for radial-depth cueing reovirus particles and other macromolecular structures determined by cryoelectron microscopy and image reconstruction. J. Struct. Biol.* **120**, 11–21.

Stewart, M. (1988). *Computer image processing of electron micrographs of biological structures with helical symmetry. J. Electron Microsc. Tech.* **9**, 325–358.

Stewart, M. (1990). *Electron microscopy of biological macromolecules: frozen hydrated methods and computer image processing.* In *Modern microscopies: techniques and applications*, edited by P. J. Duke & A. G. Michette, pp. 9–39. New York: Plenum Press.

Stewart, P. L., Chiu, C. Y., Huang, S., Muir, T., Zhao, Y., Chait, B., Mathias, P. & Nemerow, G. R. (1997). *Cryo-EM visualization of an exposed RGD epitope on adenovirus that escapes antibody neutralization. EMBO J.* **16**, 1189–1198.

Stewart, P. L., Fuller, S. D. & Burnett, R. M. (1993). *Difference imaging of adenovirus: bridging the resolution gap between X-ray crystallography and electron microscopy. EMBO J.* **12**, 2589–2599.

19.6 (*cont.*)

Subramaniam, S., Gerstein, M., Oesterhelt, D. & Henderson, R. (1993). *Electron diffraction analysis of structural changes in the photocycle of bacteriorhodopsin. EMBO J.* **12**, 1–18.

Tao, Y., Olson, N. H., Xu, W., Anderson, D. L., Rossmann, M. G. & Baker, T. S. (1998). *Assembly of a tailed bacterial virus and its genome release studied in three dimensions. Cell*, **95**, 431–437.

Taveau, J.-C. (1996). *Presentation of the SIGMA software: software of imagery and graphics for molecular architecture. J. Struct. Biol.* **116**, 223–229.

Taylor, K. A. & Glaeser, R. M. (1974). *Electron diffraction of frozen, hydrated protein crystals. Science*, **186**, 1036–1037.

Taylor, K. A. & Glaeser, R. M. (1976). *Electron microscopy of frozen hydrated biological specimens. J. Ultrastruct. Res.* **55**, 448–456.

Taylor, K. A., Tang, J., Cheng, Y. & Winkler, H. (1997). *The use of electron tomography for structural analysis of disordered protein arrays. J. Struct. Biol.* **120**, 372–386.

Thuman-Commike, P. A. & Chiu, W. (1996). *PTOOL: a software package for the selection of particles from electron cryomicroscopy spot-scan images. J. Struct. Biol.* **116**, 41–47.

Toyoshima, C. & Unwin, N. (1990). *Three-dimensional structure of the acetylcholine receptor by cryoelectron microscopy and helical image reconstruction. J. Cell Biol.* **111**, 2623–2635.

Toyoshima, C., Yonekura, K. & Sasabe, H. (1993). *Contrast transfer for frozen-hydrated specimens. II. Amplitude contrast at very low frequencies. Ultramicroscopy*, **48**, 165–176.

Trachtenberg, S. (1998). *A fast-freezing device with a retractable environmental chamber, suitable for kinetic cryo-electron microscopy studies. J. Struct. Biol.* **123**, 45–55.

Trinick, J. & Cooper, J. (1990). *Concentration of solutes during preparation of aqueous suspensions for cryo-electron microscopy. J. Microsc.* **159**, 215–222.

Trus, B. L., Roden, R. B. S., Greenstone, H. L., Vrhel, M., Schiller, J. T. & Booy, F. P. (1997). *Novel structural features of bovine papillomavirus capsid revealed by a three-dimensional reconstruction to 9 Å resolution. Nature Struct. Biol.* **4**, 413–420.

Unger, V. M., Kumar, N. M., Gilula, N. B. & Yeager, M. (1999). *Three-dimensional structure of a recombinant gap junction membrane channel. Science*, **283**, 1176–1180.

Unser, M., Trus, B. L., Frank, J. & Steven, A. C. (1989). *The spectral signal-to-noise ratio resolution criterion: computational efficiency and statistical precision. Ultramicroscopy*, **30**, 429–434.

Unwin, N. (1993). *Nicotinic acetylcholine receptor at 9 Å resolution. J. Mol. Biol.* **229**, 1101–1124.

Unwin, N. (1995). *Acetylcholine receptor channel imaged in the open state. Nature (London)*, **373**, 37–43.

Unwin, P. N. T. & Henderson, R. (1975). *Molecular structure determination by electron microscopy of unstained crystalline specimens. J. Mol. Biol.* **94**, 425–440.

Valpuesta, J. M., Carrascosa, J. L. & Henderson, R. (1994). *Analysis of electron microscope images and electron diffraction patterns of thin crystals of Φ29 connectors in ice. J. Mol. Biol.* **240**, 281–287.

Vénien-Bryan, C. & Fuller, S. D. (1994). *The organization of the spike complex of Semliki forest virus. J. Mol. Biol.* **236**, 572–583.

Vigers, G. P. A., Crowther, R. A. & Pearse, B. M. F. (1986). *Three-dimensional structure of clathrin cages in ice. EMBO J.* **5**, 529–534.

Volkmann, N. & Hanein, D. (1999). *Quantitative fitting of atomic models into observed densities derived by electron microscopy. J. Struct. Biol.* **125**, 176–184.

Wade, R. H. (1992). *A brief look at imaging and contrast transfer. Ultramicroscopy*, **46**, 145–156.

Wade, R. H. & Frank, J. (1977). *Electron microscope transfer functions for partially coherent axial illumination and chromatic defocus spread. Optik*, **49**, 81–92.

Walker, M., Zhang, X.-Z., Jiang, W., Trinick, J. & White, H. D. (1999). *Observation of transient disorder during myosin subfragment-1 binding to actin by stopped-flow fluorescence and millisecond time resolution electron cryomicroscopy: evidence that the start of the crossbridge power stroke in muscle has variable geometry. Proc. Natl Acad. Sci. USA*, **96**, 465–470.

Walz, J., Tamura, T., Tamura, N., Grimm, R., Baumeister, W. & Koster, A. J. (1997). *Tricorn protease exists as an icosahedral supermolecule in vivo. Mol. Cell*, **1**, 59–65.

Walz, T. & Grigorieff, N. (1998). *Electron crystallography of two-dimensional crystals of membrane proteins. J. Struct. Biol.* **121**, 142–161.

White, H. D., Walker, M. L. & Trinick, J. (1998). *A computer-controlled spraying-freezing apparatus for millisecond time-resolution electron cryomicroscopy. J. Struct. Biol.* **121**, 306–313.

Wikoff, W. R., Wang, G., Parrish, C. R., Cheng, R. H., Strassheim, M. L., Baker, T. S. & Rossmann, M. G. (1994). *The structure of a neutralized virus: canine parvovirus complexed with neutralizing antibody fragment. Structure*, **2**, 595–607.

Wilson-Kubalek, E. M., Brown, R. E., Celia, H. & Milligan, R. A. (1998). *Lipid nanotubes as substrates for helical crystallization of macromolecules. Proc. Natl Acad. Sci. USA*, **95**, 8040–8045.

Winkelmann, D. A., Baker, T. S. & Rayment, I. (1991). *Three-dimensional structure of myosin subfragment-1 from electron microscopy of sectioned crystals. J. Cell Biol.* **114**, 701–713.

Winkler, H., Reedy, M. C., Reedy, M. K., Tregear, R. & Taylor, K. A. (1996). *Three-dimensional structure of nucleotide-bearing crossbridges in situ: oblique section reconstruction of insect flight muscle in AMPPNP at 23°C. J. Mol. Biol.* **264**, 302–322.

Winkler, H. & Taylor, K. A. (1996). *Software for 3-D reconstruction from images of oblique sections through 3-D crystals. J. Struct. Biol.* **116**, 241–247.

Wriggers, W., Milligan, R. A. & McCammon, J. A. (1999). *Situs: a package for docking crystal structures into low-resolution maps from electron microscopy. J. Struct. Biol.* **125**, 185–195.

Wynne, S. A., Crowther, R. A. & Leslie, A. G. W. (1999). *Crystal structure of the hepatitis B virus capsid. Mol. Cell*, **3**, 771–780.

Yeager, M., Berriman, J. A., Baker, T. S. & Bellamy, A. R. (1994). *Three-dimensional structure of the rotavirus hemagglutinin VP4 by cryo-electron microscopy and difference map analysis. EMBO J.* **13**, 1011–1018.

Yeager, M., Unger, V. M. & Mitra, A. K. (1999). *Three-dimensional structure of membrane proteins determined by two-dimensional crystallization, electron cryomicroscopy, and image analysis. Methods Enzymol.* **294**, 135–180.

Yoshimura, H., Matsumoto, M., Endo, S. & Nagayama, K. (1990). *Two-dimensional crystallization of proteins on mercury. Ultramicroscopy*, **32**, 265–274.

Zemlin, F. (1989). *Dynamic focusing for recording images from tilted samples in small-spot scanning with a transmission electron microscope. J. Electron Microsc. Tech.* **11**, 251–257.

Zemlin, F. (1992). *Desired features of a cryoelectron microscope for the electron crystallography of biological material. Ultramicroscopy*, **46**, 25–32.

Zemlin, F. (1994). *Expected contribution of the field-emission gun to high-resolution transmission electron microscopy. Micron*, **25**, 223–226.

Zemlin, F., Beckmann, E. & van der Mast, K. D. (1996). *A 200 kV electron microscope with Schottky field emitter and a helium-cooled superconducting objective lens. Ultramicroscopy*, **63**, 227–238.

Zhao, X., Fox, J. M., Olson, N. H., Baker, T. S. & Young, M. J. (1995). *In vitro assembly of cowpea chlorotic mottle virus from coat protein expressed in Escherichia coli and in vitro-transcribed viral cDNA. Virology*, **207**, 486–494.

Zhou, Z. H., Chen, D. H., Jakana, J., Rixon, F. J. & Chiu, W. (1999). *Visualization of tegument–capsid interactions and DNA in intact herpes simplex virus type 1 virions. J. Virol.* **73**, 3210–3218.

Zhou, Z. H. & Chiu, W. (1993). *Prospects for using an IVEM with a FEG for imaging macromolecules towards atomic resolution. Ultramicroscopy*, **49**, 407–416.

Zhou, Z. H., Chiu, W., Haskell, K., Spears, H. J., Jakana, J., Rixon, F. J. & Scott, L. R. (1998). *Refinement of herpesvirus B-capsid structure on parallel supercomputers. Biophys. J.* **74**, 576–588.

Zhou, Z. H., Hardt, S., Wang, B., Sherman, M. B., Jakana, J. & Chiu, W. (1996). *CTF determination of images of ice-embedded single particles using a graphics interface. J. Struct. Biol.* **116**, 216–222.

Zhou, Z. H., Macnab, S. J., Jakana, J., Scott, L. R., Chiu, W. & Rixon, F. J. (1998). *Identification of the sites of interaction between the scaffold and outer shell in herpes simplex virus-1 capsids by difference electron imaging. Proc. Natl Acad. Sci. USA*, **95**, 2778–2783.

Zhou, Z. H., Prasad, B. V. V., Jakana, J., Rixon, F. J. & Chiu, W. (1994). *Protein subunit structures in the herpes simplex virus A-capsid determined from 400 kV spot-scan electron cryomicroscopy. J. Mol. Biol.* **242**, 456–469.

Zhu, J., Penczek, P. A., Schroder, R. & Frank, J. (1997). *Three-dimensional reconstruction with contrast transfer function correction from energy-filtered cryoelectron micrographs: procedure and application to the 70S Escherichia coli ribosome. J. Struct. Biol.* **118**, 197–219.

19.7

Banci, L., Bertini, I., Cremonini, M. A., Gori-Savellini, G., Luchinat, C., Wüthrich, K. & Güntert, P. (1998). *PSEUDYANA for NMR structure calculation of paramagnetic metalloproteins using torsion angle molecular dynamics. J. Biomol. NMR*, **12**, 553–557.

Bax, A. & Grzesiek, S. (1993). *Methodological advances in protein NMR. Acc. Chem. Res.* **26**, 131–138.

Billeter, M. (1992). *Comparison of protein structures determined by NMR in solution and by X-ray diffraction in single-crystals. Q. Rev. Biophys.* **25**, 325–377.

Billeter, M., Braun, W. & Wüthrich, K. (1982). *Sequential resonance assignments in protein ^1H nuclear magnetic resonance spectra: computation of sterically allowed proton–proton distances and statistical analysis of proton–proton distances in single crystal protein conformations. J. Mol. Biol.* **155**, 321–346.

Billeter, M., Güntert, P., Luginbühl, P. & Wüthrich, K. (1996). *Hydration and DNA recognition by homeodomains. Cell*, **85**, 1057–1065.

Braun, W., Epp, O., Wüthrich, K. & Huber, R. (1989). *Solution of the phase problem in the X-ray diffraction method for proteins with the nuclear magnetic resonance solution structure as initial model. J. Mol. Biol.* **206**, 669–676.

Brünger, A. T., Clore, G. M., Gronenborn, A. M. & Karplus, M. (1986). *Three-dimensional structure of proteins determined by molecular dynamics with interproton distance restraints. Application to crambin. Proc. Natl Acad. Sci. USA*, **83**, 3801–3805.

Brunne, R. M., Liepinsh, E., Otting, G., Wüthrich, K. & van Gunsteren, W. F. (1993). *Hydration of proteins. A comparison of experimental residence times of water molecules solvating the bovine pancreatic trypsin inhibitor with theoretical model calculations. J. Mol. Biol.* **231**, 1040–1048.

Brüschweiler, R. & Wright, P. E. (1994). *Water self-diffusion model for protein–water NMR cross relaxation. Chem. Phys. Lett.* **229**, 75–81.

Cavanagh, J., Fairbrother, W. J., Palmer, A. G. III & Skelton, N. J. (1996). *Protein NMR spectroscopy, principles and practice*. New York: Academic Press.

Denisov, V. P., Peters, J., Hörlein, H. D. & Halle, B. (1996). *Using buried water molecules to explore the energy landscape of proteins. Nature Struct. Biol.* **3**, 505–509.

Dubs, A., Wagner, G. & Wüthrich, K. (1979). *Individual assignments of amide proton resonances in the proton NMR spectrum of the basic pancreatic trypsin inhibitor. Biochim. Biophys. Acta*, **577**, 177–194.

Ernst, R. R., Bodenhausen, G. & Wokaun, A. (1987). *Principles of nuclear magnetic resonance in one and two dimensions*. Oxford: Clarendon Press.

Güntert, P., Berndt, K. D. & Wüthrich, K. (1993). *The program ASNO for computer-supported collection of NOE upper distance constraints as input for protein structure determination. J. Biomol. NMR*, **3**, 601–606.

Güntert, P., Mumenthaler, C. & Wüthrich, K. (1997). *Torsion angle dynamics for NMR structure calculation with the new program DYANA. J. Mol. Biol.* **273**, 283–298.

Havel, T. F. & Wüthrich, K. (1985). *An evaluation of the combined use of nuclear magnetic resonance and distance geometry for the determination of protein conformations in solution. J. Mol. Biol.* **182**, 281–294.

Kallen, J., Spitzfaden, C., Zurini, M. G. M., Wider, G., Widmer, H., Wüthrich, K. & Walkinshaw, M. D. (1991). *Structure of human cyclophilin and its binding site for cyclosporin A determined by X-ray crystallography and NMR spectroscopy. Nature (London)*, **353**, 276–279.

Kay, L. E. & Gardner, K. H. (1997). *Solution NMR spectroscopy beyond 25 kDa. Curr. Opin. Struct. Biol.* **7**, 722–731.

Otting, G., Liepinsh, E. & Wüthrich, K. (1991). *Protein hydration in aqueous solution. Science*, **254**, 974–980.

Otting, G., Liepinsh, E. & Wüthrich, K. (1993). *Disulfide bond isomerization in BPTI and BPTI(G36S): an NMR study of correlated mobility in proteins. Biochemistry*, **32**, 3571–3582.

Peng, J. W. & Wagner, G. (1992). *Mapping of spectral density functions using heteronuclear NMR relaxation measurements. J. Magn. Reson.* **98**, 308–332.

Pervushin, K., Riek, R., Wider, G. & Wüthrich, K. (1997). *Attenuated T_2 relaxation by mutual cancellation of dipole–dipole coupling and chemical shift anisotropy indicates an avenue to NMR structures of very large biological macromolecules in solution. Proc. Natl Acad. Sci. USA*, **94**, 12366–12371.

Qian, Y. Q., Billeter, M., Otting, G., Müller, M., Gehring, W. J. & Wüthrich, K. (1989). *The structure of the Antennapedia homeodomain determined by NMR spectroscopy in solution: comparison with prokaryotic repressors. Cell*, **59**, 573–580.

Riek, R., Wider, G., Pervushin, K. & Wüthrich, K. (1999). *Polarization transfer by cross-correlated relaxation in solution NMR with very large molecules. Proc. Natl Acad. Sci. USA*, **96**, 4918–4923.

Salzmann, M., Pervushin, K., Wider, G., Senn, H. & Wüthrich, K. (1998). *TROSY in triple-resonance experiments: new perspectives for sequential NMR assignment of large proteins. Proc. Natl Acad. Sci. USA*, **95**, 13585–13590.

Tjandra, N. & Bax, A. (1997). *Direct measurement of distances and angles in biomolecules by NMR in dilute liquid crystalline medium. Science*, **278**, 1111–1114.

Wagner, G. (1980). *Activation volumes for the rotational motion of interior aromatic rings in globular proteins determined by high resolution ^1H NMR at variable pressure. FEBS Lett.* **112**, 280–284.

Wagner, G. & Wüthrich, K. (1982). *Sequential resonance assignments in protein ^1H nuclear magnetic resonance spectra: basic pancreatic trypsin inhibitor. J. Mol. Biol.* **155**, 347–366.

Wishart, D. S., Sykes, B. D. & Richards, F. M. (1991). *Relationship between nuclear-magnetic-resonance chemical shift and protein secondary structure. J. Mol. Biol.* **222**, 311–333.

Wüthrich, K. (1976). *NMR in biological research: peptides and proteins*. Amsterdam: North Holland.

Wüthrich, K. (1986). *NMR of proteins and nucleic acids*. New York: Wiley.

Wüthrich, K. (1989). *Protein structure determination in solution by nuclear magnetic resonance spectroscopy. Science*, **243**, 45–50.

Wüthrich, K. (1995). *NMR – this other method for protein and nucleic acid structure determination. Acta Cryst.* D**51**, 249–270.

Wüthrich, K., Billeter, M. & Braun, W. (1984). *Polypeptide secondary structure determination by nuclear magnetic resonance observation of short proton–proton distances. J. Mol. Biol.* **180**, 715–740.

Wüthrich, K. & Wagner, G. (1975). *NMR investigations of the dynamics of the aromatic amino acid residues in the basic pancreatic trypsin inhibitor. FEBS Lett.* **50**, 265–268.